Finite strain primal interface formulation with consistently evolving stabilization[‡]

Timothy J. Truster[1], Pinlei Chen[2] and Arif Masud[2,*,†]

[1]*Department of Civil and Environmental Engineering, University of Tennessee, Knoxville, 318 John D. Tickle Engineering Building, Knoxville, TN 37921, USA*
[2]*Department of Civil and Environmental Engineering, University of Illinois at Urbana-Champaign, 3129E Newmark Civil Engineering Laboratory, MC-250, Urbana, IL 61801-2352, USA*

SUMMARY

A stabilized discontinuous Galerkin method is developed for general hyperelastic materials at finite strains. Starting from a mixed method incorporating Lagrange multipliers along the interface, the displacement formulation is systematically derived through a variational multiscale approach whereby the numerical fine scales are modeled via edge bubble functions. Analytical expressions that are free from user-defined parameters arise for the weighted numerical flux and stability tensor. In particular, the specific form taken by these derived quantities naturally accounts for evolving geometric nonlinearity as well as discontinuous material properties. The method is applicable both to problems containing nonconforming meshes or different element types at specific interfaces and to problems consisting of fully discontinuous numerical approximations. Representative numerical tests involving large strains and rotations are performed to confirm the robustness of the method. Copyright © 2015 John Wiley & Sons, Ltd.

1. INTRODUCTION

The discontinuous Galerkin (DG) method provides an attractive technique for imposing strong or weak discontinuity conditions efficiently within computational models. The approach yields consistent formulations compared with the penalty method and does not introduce additional unknown fields as required in Lagrange multiplier methods. Examples from solid mechanics include the relaxation of continuity across element boundaries to treat incompressibility [1, 2] as well as the modeling of material interfaces both along element boundaries [3] and within element interiors [4, 5].

Some of the earliest methods applying discontinuous approximations to solve boundary value problems include the approaches for hyperbolic problems by Johnson [6] and for elliptical problems by Arnold [7]. The latter is commonly termed as an interior penalty method, which was influenced by a method proposed by Nitsche [8] for weakly imposed Dirichlet boundary conditions. Subsequently, the Nitsche method has been applied in the area of solid mechanics to treat incompressibility [9] and to handle embedded interfaces and cracks within the FE mesh [4, 5, 10]. Similar applications exist in the context of fluid mechanics, such as the weak imposition of no-slip conditions for wall bounded flows [11]. An extensive summary of the DG method for linear problems is given by Arnold *et al.* [12].

---

*Correspondence to: Arif Masud, Department of Civil and Environmental Engineering, University of Illinois at Urbana-Champaign, 3129E Newmark Civil Engineering Laboratory, MC-250, Urbana, IL 61801-2352, USA.
†E-mail: amasud@illinois.edu
‡Dedicated to Professor Ted Belytschko on the occasion of his 70th birthday.

The key factors impacting the robustness and efficiency of the DG method are the design of the so-called numerical flux and the penalty or stabilization parameter. Regarding the penalty parameter, studies for embedded interface problems [5] as well as discontinuous discrete approximations [2, 13] have shown that selecting a value outside of an optimal range leads to issues with accuracy and stability. Choosing a value that is too low leads to loss of coercivity and results in an ill-posed discrete problem. On the other hand, choosing a value that is too high leads to ill conditioning in the stiffness matrix as well as to overly strict enforcement of the displacement jump condition. When the jump condition is strictly enforced, the computed response approaches that of a continuous Galerkin method, and the rationale for employing DG is lost. Dimensional analyses indicate that the stability parameter is a function of the element geometry, polynomial order, material properties, and the local interface topology; however, its magnitude can be elusive. The classical approach in the context of linear problems is to estimate the parameter through eigenvalue analyses [14, 15]. More recently, in the context of embedded interface problems [4], the values of the parameter for linear simplex elements were determined by conducting a mathematical analysis of the coercivity condition. In particular, definitions for the numerical flux and penalty parameter that involved a weighting of the element size and material properties across the interface emerged. In contrast, the standard definition for the numerical flux in DG methods [12] assumes an equal weighting of the flux field from each side of the interface, which is postulated based on the assumption of mesh uniformity. Other interface methods have previously employed either area weighting [16] or stiffness weighting [5] alone. Additional techniques for defining the penalty parameter for linear problems include developments using bubble functions [17, 18] and the variational multiscale (VMS) method [19].

For the case of finite strain solid mechanics problems, the design of the stability parameter becomes more delicate because the material constitutive law evolves with the deformation, thereby implying that the stability estimates also evolve. In recent years, multiple nonlinear DG methods have been proposed for solving elasticity and plasticity problems, for which we cite [2, 10, 20–26]. Across each of these studies, the value of the penalty parameter was treated as a user-defined parameter that was calibrated for particular numerical test cases; only a few mathematical analyses have been undertaken for the nonlinear problem [27, 28]. However other researchers have shown [20, 27] that prescribing a value a priori may not lead to a robust method, particularly when the simulated response involves large deformations or material instability. These authors proposed an adaptive yet heuristic method for evolving the penalty parameter separately along each element interface by evaluating the minimum eigenvalue of the acoustic tensor of material moduli. These studies indicate that the increasing degrees of complexity encountered in finite strain problems call for a sophistication of the underlying variational formulation of the DG method. In particular, the lack of a well-defined value for the penalty parameter has been a cause for concern that has limited the adoption of this method by the general research community [4].

In this work, we set out to derive a DG method for large strain kinematics in which computable expressions for the numerical flux and penalty parameter naturally arise. The derivation parallels our previous work for linear elasticity [19], where an underlying Lagrange multiplier formulation for the interface constraints is converted into a primal formulation. By viewing the problem in light of the VMS philosophy, the mixed formulation gives rise to numerical fine scales locally at the interface due to sources of instability such as mesh nonconformity or significant material mismatch. Herein, the associated fine-scale weak form is approximated locally over segments of the interface by representing the fine-scale fields using edge bubble functions, resulting in fine-scale models that account for the constitutive response and element geometry on each side of the interface. By embedding these models into the coarse-scale weak form, a displacement-based interface formulation is obtained through local condensation of the multiplier field. The terms in the formulation share a resemblance with nonlinear interior penalty DG methods, such as the interface method presented in [10]. However, the present formulation contains consistent definitions for the penalty parameter along with a weighted numerical flux that are directly linked to the fine-scale models. Namely, the value of the penalty parameter and flux weights can vary spatially along the interface from element to element because of the local characteristics of the fine-scale models, a feature that is reported in [19].

A distinguishing feature in the present context is that the fine-scale models evolve with the material and geometric nonlinearity exhibited in the vicinity of the interface. Therefore, through their dependence on the fine-scale models, the algorithmic interface parameters are updated automatically in a consistent fashion as the nonlinear problem evolves. The resulting method is free from tunable parameters and capable of handling nonconforming meshes and material mismatch along discrete interfaces undergoing general large deformations. A straightforward generalization of the derivations enables a fully discontinuous functional approximation to be employed throughout the domain in line with the traditional meaning for discontinuous Galerkin; see, for example, [2, 27]. A series of numerical tests are conducted employing nonconforming interfaces or discontinuous approximations across a spectrum of deformation modes to assess the stability and robustness of the method.

In the following section, we begin by discussing the underlying Lagrange multiplier formulation for imposing continuity across interfaces in the finite deformation context. The derivation of the stabilized interface formulation employing the VMS method is presented in Section 3. The approach is subsequently extended to domains containing multiple interfaces in Section 4. Key aspects regarding the implementation of the fine-scale models are discussed in Section 5. In Section 6, multiple benchmark problems are considered, including an error convergence analysis. Finally, we give concluding remarks in Section 7.

2. GOVERNING EQUATIONS AND MIXED INTERFACIAL WEAK FORM

As a model problem, we consider a deformable body $\Omega \subset \mathbb{R}^{n_{sd}}$ that is cut into two disjoint regions $\Omega^{(1)}$ and $\Omega^{(2)}$ by an interface of interest Γ_I; an illustration is given in Figure 1(a) and 1(b), in which the regions are visibly separated for clarity. The case of multiple interfaces, such as those encountered in the context of DG methods, is accommodated by a straightforward generalization of the following developments. Throughout, we denote quantities with counterparts in both regions by a superscript (α), where α takes the value 1 or 2. Additionally, we suppress the superscripts in some expressions that apply equally to both regions in order to simplify the presentation.

We denote points in the reference configuration by $X \in \Omega^{(1)} \cup \Omega^{(2)}$ and their corresponding images in the current configuration by x. The current position of each region $\Omega^{(\alpha)}$ at time t is given by the image of all points $X \in \Omega^{(\alpha)}$ under the deformation map $\phi^{(\alpha)}(X, t)$ such that $x(X, t) = \phi^{(\alpha)}(X, t)$. An example of the deformed configuration is depicted in Figure 1(c). We also define the displacement field associated with the deformation $\phi^{(\alpha)}$ as $u^{(\alpha)}(X, t) = x(X, t) - X$. Finally, the deformation gradient $F^{(\alpha)}(X, t)$ emanating from $\phi^{(\alpha)}(X, t)$ is obtained as follows:

$$F(X, t) \equiv \frac{\partial x}{\partial X} = \operatorname{GRAD} x \tag{1}$$
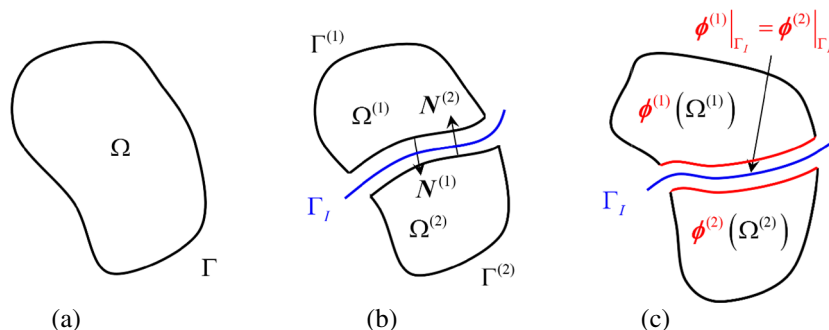

Figure 1. (a) Single domain Ω; (b) imposition of interface Γ_I; (c) deformed configuration generated by $\phi^{(1)}$ and $\phi^{(2)}$.

Although the deformations $\boldsymbol{\phi}^{(\alpha)}$ could in general take distinct values along Γ_I, we desire that the domains $\Omega^{(1)}$ and $\Omega^{(2)}$ remain compatible and equilibrated with respect to each other for all time such that the image of the body $\Omega = \Omega^{(1)} \cup \Omega^{(2)}$ remains contiguous. Namely, as shown in Figure 1(c), while the interface may deform and translate, these motions are subject to the constraint that the mapped portions of the boundary $\boldsymbol{\phi}^{(\alpha)}\left(\Gamma^{(\alpha)} \cap \Gamma_I\right)$ must coincide and conform within this zone. Thus, the equilibrium equation and boundary conditions for each region $\Omega^{(\alpha)}$ are combined with the statements of deformation continuity and balance of tractions along Γ_I to yield the following system of equations for the composite domain Ω:

$$\text{DIV } \boldsymbol{P}^{(\alpha)}\left(\boldsymbol{F}^{(\alpha)}\right) + \rho_o^{(\alpha)} \boldsymbol{B}^{(\alpha)} = \boldsymbol{0} \qquad \text{in } \Omega^{(\alpha)}, \ \alpha = 1, 2 \tag{2}$$

$$\boldsymbol{\phi}^{(\alpha)} = \boldsymbol{X}^{(\alpha)} \qquad \text{on } \Gamma^{(\alpha)} \backslash \Gamma_I, \ \alpha = 1, 2 \tag{3}$$

$$\boldsymbol{\phi}^{(1)} - \boldsymbol{\phi}^{(2)} = \boldsymbol{0} \qquad \text{on } \Gamma_I \tag{4}$$

$$\boldsymbol{P}^{(1)} \cdot \boldsymbol{N}^{(1)} + \boldsymbol{P}^{(2)} \cdot \boldsymbol{N}^{(2)} = \boldsymbol{0} \qquad \text{on } \Gamma_I \tag{5}$$

where $\boldsymbol{B}^{(\alpha)}$ is the mass-specific body force, $\rho_o^{(\alpha)}$ is the referential mass density, $\text{DIV}(\cdot) = \text{tr}\left[\text{GRAD}(\cdot)\right]$ is the material divergence operator, and $\boldsymbol{N}^{(\alpha)}$ is the unit outward normal on the region boundary $\Gamma^{(\alpha)}$. The first Piola–Kirchhoff stress tensor is denoted by $\boldsymbol{P}^{(\alpha)}$, and we restrict our current focus to hyperelastic materials such that $\boldsymbol{P}^{(\alpha)}$ is derived from an associated strain energy density function $W^{(\alpha)}\left(\boldsymbol{F}^{(\alpha)}; \boldsymbol{X}\right)$:

$$\boldsymbol{P}^{(\alpha)} = \frac{\partial W^{(\alpha)}}{\partial \boldsymbol{F}^{(\alpha)}} \tag{6}$$

We assume for simplicity that $W^{(\alpha)}$ is spatially homogeneous, that is, $W^{(\alpha)} = W^{(\alpha)}\left(\boldsymbol{F}^{(\alpha)}\right)$; however, we in general allow distinct material models such that $W^{(1)}(\boldsymbol{F}) \neq W^{(2)}(\boldsymbol{F})$. Additionally, we have prescribed homogeneous Dirichlet conditions on the external boundaries in order to focus on the interfacial contributions in the following developments; the results are easily extended to treat nonhomogeneous boundary conditions or Neumann (traction) conditions.

Two classical techniques exist for weakly imposing the interface conditions (4)-(5): the penalty method and the Lagrange multiplier method. While the penalty method is conceptually simple and easy to implement, it suffers from the inconsistent enforcement of the traction balance (5), which is resolved only in the limit as the penalty parameter approaches infinity. Also, overly large values of the penalty parameter yield ill conditioning in the global stiffness matrix, which can be detrimental to the stability of the nonlinear solution procedure [20, 29] or of the iterative linear equation solver [13]. In contrast, the Lagrange multiplier technique consistently enforces (4)-(5) through the incorporation of an auxiliary unknown field $\boldsymbol{\lambda}$ at the interface. Thus, we adopt this technique as the starting point for developing our proposed formulation. The associated weak form is stated as follows: find $\left\{\boldsymbol{\phi}^{(1)}, \boldsymbol{\phi}^{(2)}, \boldsymbol{\lambda}\right\} \in \mathcal{S}^{(1)} \times \mathcal{S}^{(2)} \times \mathcal{Q}$ such that for all $\left\{\boldsymbol{\eta}_o^{(1)}, \boldsymbol{\eta}_o^{(2)}, \boldsymbol{\mu}\right\} \in \mathcal{V}^{(1)} \times \mathcal{V}^{(2)} \times \mathcal{Q}$:

$$\sum_{\alpha=1}^{2} \int_{\Omega^{(\alpha)}} \text{GRAD } \boldsymbol{\eta}_o^{(\alpha)} : \boldsymbol{P}^{(\alpha)} \mathrm{d}V - \sum_{\alpha=1}^{2} \int_{\Omega^{(\alpha)}} \rho_o^{(\alpha)} \boldsymbol{B}^{(\alpha)} \cdot \boldsymbol{\eta}_o^{(\alpha)} \mathrm{d}V - \int_{\Gamma_I} \boldsymbol{\lambda} \cdot [\![\boldsymbol{\eta}_o]\!] \mathrm{d}A = 0 \tag{7}$$

$$- \int_{\Gamma_I} \boldsymbol{\mu} \cdot [\![\boldsymbol{\phi}]\!] \mathrm{d}A = 0 \tag{8}$$

Herein, the Lagrange multiplier field $\boldsymbol{\lambda}$ has the connotation of the traction field on Γ_I derived from region $\Omega^{(1)}$. Also, we have introduced the jump operator $[\![\cdot]\!] = (\cdot)^{(1)} - (\cdot)^{(2)}$ defined for vector-valued fields on interface Γ_I. Although this definition depends on the ordering of the domains as

in [19], the final weak form obtained at the completion of the derivations is independent of the ordering. We specify the functional spaces contained in (7)-(8) as follows:

$$\mathcal{S}^{(\alpha)} = \left\{ \boldsymbol{\phi}^{(\alpha)} \,\middle|\, \boldsymbol{\phi}^{(\alpha)} \in \left[H^1 \left(\Omega^{(\alpha)} \right) \right]^{n_{\mathrm{sd}}}, \det \left(\boldsymbol{F}^{(\alpha)} \left(\boldsymbol{\phi}^{(\alpha)} \right) \right) > 0, \; \boldsymbol{\phi}^{(\alpha)} \Big|_{\Gamma^{(\alpha)} \backslash \Gamma_I} = \boldsymbol{X}^{(\alpha)} \right\} \qquad (9)$$

$$\mathcal{V}^{(\alpha)} = \left\{ \boldsymbol{\eta}_o^{(\alpha)} \,\middle|\, \boldsymbol{\eta}_o^{(\alpha)} \in \left[H_o^1 \left(\Omega^{(\alpha)} \right) \right]^{n_{\mathrm{sd}}}, \boldsymbol{\eta}_o^{(\alpha)} \Big|_{\Gamma^{(\alpha)} \backslash \Gamma_I} = \boldsymbol{0} \right\} \qquad (10)$$

$$\mathcal{Q} = \left\{ \boldsymbol{\lambda} \,\middle|\, \boldsymbol{\lambda} \in \left[H^{-\frac{1}{2}} (\Gamma_I) \right]^{n_{\mathrm{sd}}} \right\} \qquad (11)$$

An alternate viewpoint for obtaining expressions (7)-(8) is through finding the saddle point $\left\{ \boldsymbol{\phi}^{(1)}, \boldsymbol{\phi}^{(2)}, \boldsymbol{\lambda} \right\}$ of the following interface potential functional (see e.g., [30]):

$$\Pi \left(\boldsymbol{\phi}^{(1)}, \boldsymbol{\phi}^{(2)}, \boldsymbol{\lambda} \right) = \sum_{\alpha=1}^{2} \left[\int_{\Omega^{(\alpha)}} W^{(\alpha)} \left(\boldsymbol{F}^{(\alpha)} \right) \mathrm{d}V - \int_{\Omega^{(\alpha)}} \rho_o^{(\alpha)} \boldsymbol{B}^{(\alpha)} \cdot \boldsymbol{\phi}^{(\alpha)} \mathrm{d}V \right] - \int_{\Gamma_I} \boldsymbol{\lambda} \cdot [\![\boldsymbol{\phi}^{(\alpha)}]\!] \, \mathrm{d}A$$

$$(12)$$

This expression, which clearly possesses an underlying variational structure, will serve as the point of departure for the developments in the following sections. Preserving the characteristics of this structure will be an important concern through the derivations that follow.

3. MULTISCALE DECOMPOSITION

Our objective at this point is to convert the preceding Lagrange multiplier formulation into a stabilized pure-displacement method reminiscent of the standard DG method. By doing so, we can avoid the two main shortcomings of the Lagrange multiplier method, namely the inclusion of additional unknowns to solve for and the stability issues associated with the mixed field problems. While the mixed weak form (7)-(8) is well posed in the continuum setting for most classes of deformations, the question of stability is more delicate for the discrete counterpart. Specifically, the choice of approximation for the deformation and multiplier spaces must satisfy an inf-sup condition, commonly termed as the Babuška–Brezzi condition [31], the analysis of which can be difficult in the nonlinear setting [32, 33]. Additional complications for selecting appropriate multipliers spaces arise when the discretizations of regions $\Omega^{(1)}$ and $\Omega^{(2)}$ are nonconforming. To avoid these issues, we employ the general framework of Masud and Scovazzi [34] for mathematically nonsmooth problems and consistently combine the stabilized linear DG methods presented by Truster and Masud [19] with the stabilized finite deformation formulation of Masud and Truster [35] to derive a stabilized finite strain interface method. The underlying philosophy common to each of these works is the VMS method [36], which has served as a platform for developing methods with enhanced stability across solid mechanics [9, 35, 37, 38] and fluid mechanics [11, 39, 40].

The key idea of the VMS philosophy is that the solution field is decomposed into coarse scales, often associated with the discrete function space, and fine scales, associated with the features of the solution unresolved by the discrete space. Presently, we follow [35] and assume an overlapping decomposition of the deformation map $\boldsymbol{\phi}^{(\alpha)}$ in each region $\Omega^{(\alpha)}$ consisting of a fine-scale deformation $\tilde{\boldsymbol{\phi}}^{(\alpha)}$ superimposed upon a coarse-scale deformation $\hat{\boldsymbol{\phi}}^{(\alpha)}$. This deformation can be expressed in terms of the multiscale displacement field as follows:

$$\boldsymbol{\phi} = \tilde{\boldsymbol{\phi}} \circ \hat{\boldsymbol{\phi}} = \boldsymbol{X} + \hat{\boldsymbol{u}} + \tilde{\boldsymbol{u}} \qquad (13)$$

$$\hat{\boldsymbol{\phi}}(\boldsymbol{X}) = \boldsymbol{X} + \hat{\boldsymbol{u}}(\boldsymbol{X}) \equiv \hat{\boldsymbol{x}} \qquad (14)$$

$$\tilde{\boldsymbol{\phi}} \left(\hat{\boldsymbol{x}} \right) = \hat{\boldsymbol{x}} + \tilde{\boldsymbol{u}} \left(\hat{\boldsymbol{x}} \right) \qquad (15)$$
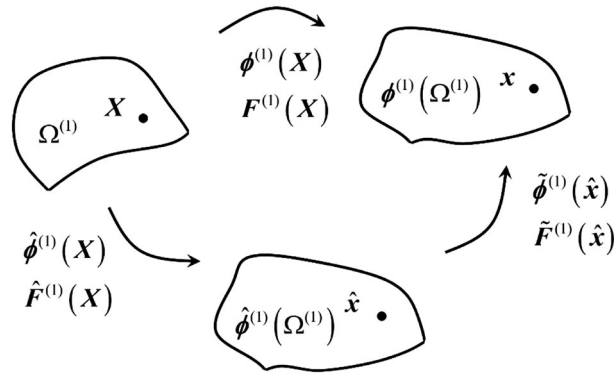
Figure 2. Multiscale composition of mappings $\tilde{\boldsymbol{\phi}}^{(1)} \circ \hat{\boldsymbol{\phi}}^{(1)}$ for region $\Omega^{(1)}$.

An illustrative example of the decomposed deformation is presented in Figure 2 for region $\Omega^{(1)}$. As highlighted in [35], a multiplicative decomposition of the deformation gradient $\boldsymbol{F}^{(\alpha)}$ follows from substituting (13) into (1):

$$\boldsymbol{F}(X) = \frac{\partial \boldsymbol{x}}{\partial \boldsymbol{X}} = \frac{\partial \boldsymbol{x}}{\partial \hat{\boldsymbol{x}}} \cdot \frac{\partial \hat{\boldsymbol{x}}}{\partial \boldsymbol{X}} = \left[\boldsymbol{I} + \frac{\partial \tilde{\boldsymbol{u}}}{\partial \hat{\boldsymbol{x}}}\right] \cdot \left[\boldsymbol{I} + \frac{\partial \hat{\boldsymbol{u}}}{\partial \boldsymbol{X}}\right] \equiv \tilde{\boldsymbol{F}} \cdot \hat{\boldsymbol{F}} \tag{16}$$

Remark:
In the context of small deformations, an additive split of the displacement field is commonly employed; see, for example, [37, 38]. However, in the finite deformation case, the total displacement is properly defined through the composition of mappings [41]. Consequently, the gradient of this composite mapping leads to a multiplicative split of the deformation gradient. Similar ideas are discussed in the context of enhanced strain formulations by Simo and Armero [42].

In our developments, we elect to represent the coarse-scale field $\hat{\boldsymbol{\phi}}^{(\alpha)}$ using piecewise continuous finite element functions in each region $\Omega^{(\alpha)}$. The fine-scale field $\tilde{\boldsymbol{\phi}}^{(\alpha)}$ is treated as being local to the interface in a manner similar to [19]; the specific functional form is discussed in the following section. For concreteness, we summarize the notation pertaining to the finite element partitions as follows. Let $\left\{\Omega_e^{(\alpha)}\right\}_{e=1}^{n_{umel}^{(\alpha)}}$ be a collection of nonoverlapping open subdomains $\Omega_e^{(\alpha)}$ called elements that cover region $\Omega^{(\alpha)} : \bigcup_{e=1}^{n_{umel}^{(\alpha)}} \bar{\Omega}_e^{(\alpha)} = \bar{\Omega}^{(\alpha)}$. Each element $\Omega_e^{(\alpha)}$ has an associated boundary $\Gamma_e^{(\alpha)}$, and we denote the union of all element interiors and boundaries by $\tilde{\Omega}^{(\alpha)}$ and $\tilde{\Gamma}^{(\alpha)}$, respectively. Also, we use the symbol $\Gamma_{I,e}^{(\alpha)}$ to indicate the intersection of an element boundary with the interface Γ_I, and the union of all such elements boundaries is denoted by $\tilde{\Gamma}_I^{(\alpha)}$. We remark that conformity of the partitions along Γ_I is not assumed; namely, an element boundary $\Gamma_{I,e}^{(2)}$ may not exist that coincides precisely with $\Gamma_{I,e}^{(1)}$ on the other side of the interface, or vice versa.

With this notation in hand, the spaces of trial coarse-scale maps $\hat{\mathcal{S}}^{(\alpha)}$ and fine-scale maps $\tilde{\mathcal{S}}^{(\alpha)}$ take the following explicit form:

$$\hat{\mathcal{S}}^{(\alpha)} = \left\{\hat{\boldsymbol{\phi}}^{(\alpha)} \left| \hat{\boldsymbol{\phi}}^{(\alpha)} \in C^o\left(\Omega^{(\alpha)}\right) \cap \mathcal{S}^{(\alpha)}, \hat{\boldsymbol{\phi}}^{(\alpha)}\right|_{\Omega_e^{(\alpha)}} \in \mathcal{P}^k\left(\Omega_e^{(\alpha)}\right) \text{ for } e = 1, \ldots, n_{umel}^{(\alpha)}\right\} \tag{17}$$

$$\tilde{\mathcal{S}}^{(\alpha)} = \left\{\tilde{\boldsymbol{\phi}}^{(\alpha)} \left| \tilde{\boldsymbol{\phi}}^{(\alpha)} = \boldsymbol{\phi}^{(\alpha)} \circ \hat{\boldsymbol{\phi}}^{-1(\alpha)} \in \mathcal{S}^{(\alpha)} \backslash \hat{\mathcal{S}}^{(\alpha)}\right.\right\} \tag{18}$$

where $\mathcal{P}^k\left(\Omega_e^{(\alpha)}\right)$ is the space of complete Lagrange polynomials of order k spanning element $\Omega_e^{(\alpha)}$. These definitions ensure a unique decomposition of the component mapping functions.

Following [19], we retain $\mathcal{Q}$ from (11) as the space of trial and test functions for the multiplier field until later in the derivation.

Returning to the interface potential functional (12) and substituting the multiscale decomposition (13), we obtain the multiscale interface potential functional:

$$\Pi\left(\hat{\boldsymbol{\phi}}^{(\alpha)},\tilde{\boldsymbol{\phi}}^{(\alpha)},\boldsymbol{\lambda}\right) = \sum_{\alpha=1}^{2}\left[\int_{\Omega^{(\alpha)}} W^{(\alpha)}\left(\boldsymbol{F}^{(\alpha)}\left(\tilde{\boldsymbol{\phi}}^{(\alpha)}\circ\hat{\boldsymbol{\phi}}^{(\alpha)}\right)\right)\mathrm{d}V - \int_{\Omega^{(\alpha)}}\rho_o^{(\alpha)}\boldsymbol{B}^{(\alpha)}\cdot\left(\tilde{\boldsymbol{\phi}}^{(\alpha)}\circ\hat{\boldsymbol{\phi}}^{(\alpha)}\right)\mathrm{d}V\right]$$
$$-\int_{\Gamma_I}\boldsymbol{\lambda}\cdot\left[\!\left[\tilde{\boldsymbol{\phi}}^{(\alpha)}\circ\hat{\boldsymbol{\phi}}^{(\alpha)}\right]\!\right]\mathrm{d}A \tag{19}$$

The corresponding multiscale weak form is obtained by taking the variation with respect to both the coarse-scale arguments $\hat{\boldsymbol{\phi}}^{(\alpha)}$ and $\boldsymbol{\lambda}$ along with the fine-scale arguments $\tilde{\boldsymbol{\phi}}^{(\alpha)}$. To facilitate this step, we record the following intermediate results from [35]:

$$\mathrm{D}_{\hat{\boldsymbol{\phi}}}\left(\tilde{\boldsymbol{\phi}}\circ\hat{\boldsymbol{\phi}}\right)\cdot\hat{\boldsymbol{\eta}}_o = \tilde{\boldsymbol{\phi}}\circ\hat{\boldsymbol{\eta}}_o \equiv \hat{\boldsymbol{\eta}}_{\tilde{\phi}}; \qquad \mathrm{D}_{\tilde{\boldsymbol{\phi}}}\left(\tilde{\boldsymbol{\phi}}\circ\hat{\boldsymbol{\phi}}\right)\cdot\tilde{\boldsymbol{\eta}}_o = \tilde{\boldsymbol{\eta}}_o\circ\hat{\boldsymbol{\phi}} \equiv \tilde{\boldsymbol{\eta}}_{\hat{\phi}} \tag{20}$$

$$\mathrm{D}_{\hat{\boldsymbol{\phi}}}\boldsymbol{F}\cdot\hat{\boldsymbol{\eta}}_o = \tilde{\boldsymbol{F}}\cdot\mathrm{GRAD}\,\hat{\boldsymbol{\eta}}_o - \mathrm{GRAD}\,\tilde{\boldsymbol{u}}\cdot\hat{\boldsymbol{F}}^{-1}\cdot\mathrm{GRAD}\,\hat{\boldsymbol{\eta}}_o = \mathrm{GRAD}\,\hat{\boldsymbol{\eta}}_o \tag{21}$$

$$\mathrm{D}_{\tilde{\boldsymbol{\phi}}}\boldsymbol{F}\cdot\tilde{\boldsymbol{\eta}}_o = \left(\widehat{\mathrm{GRAD}\tilde{\boldsymbol{\eta}}_o}\right)\cdot\hat{\boldsymbol{F}} = (\mathrm{GRAD}\,\tilde{\boldsymbol{\eta}}_o)\cdot\hat{\boldsymbol{F}}^{-1}\cdot\hat{\boldsymbol{F}} = \mathrm{GRAD}\,\tilde{\boldsymbol{\eta}}_o \tag{22}$$

where the coarse-scale and fine-scale variations in each region are denoted as $\hat{\boldsymbol{\eta}}_o^{(\alpha)}$ and $\tilde{\boldsymbol{\eta}}_o^{(\alpha)}$, respectively, and the variational (Gateaux) derivative is defined as $\mathrm{D}_{\phi}\boldsymbol{G}\cdot\boldsymbol{\eta}_o = \frac{\partial}{\partial\varepsilon}\Big|_{\varepsilon=0}\boldsymbol{G}\,(\boldsymbol{\phi}+\varepsilon\boldsymbol{\eta}_o)$ (see [35]). Note that a simplified expression (21) is obtained for the coarse-scale variation of $\boldsymbol{F}$ compared with the expression in [35] by accounting for the dependence of $\tilde{\boldsymbol{F}}$ on the coarse-scale map $\hat{\boldsymbol{\phi}}$.

Applying the variational derivative to (19) and incorporating (20)-(22) leads to the following multiscale interface problem:

Coarse-scale problem $\mathcal{C}$

$$\mathrm{D}_{\hat{\boldsymbol{\phi}}^{(\alpha)}}\left[\Pi\left(\hat{\boldsymbol{\phi}}^{(\alpha)},\tilde{\boldsymbol{\phi}}^{(\alpha)},\boldsymbol{\lambda}\right)\right]\cdot\hat{\boldsymbol{\eta}}_o^{(\alpha)} \equiv R_{\phi}\left(\hat{\boldsymbol{\eta}}_o^{(\alpha)};\hat{\boldsymbol{\phi}}^{(\alpha)},\tilde{\boldsymbol{\phi}}^{(\alpha)},\boldsymbol{\lambda}\right)$$
$$= \sum_{\alpha=1}^{2}\int_{\Omega^{(\alpha)}}\left[\mathrm{GRAD}\,\hat{\boldsymbol{\eta}}_o^{(\alpha)}:\boldsymbol{P}^{(\alpha)} - \hat{\boldsymbol{\eta}}_o^{(\alpha)}\cdot\rho_o^{(\alpha)}\boldsymbol{B}^{(\alpha)}\right]\mathrm{d}V \tag{23}$$
$$-\int_{\Gamma_I}\boldsymbol{\lambda}\cdot[\![\hat{\boldsymbol{\eta}}_o]\!]\,\mathrm{d}A = 0$$

$$\mathrm{D}_{\boldsymbol{\lambda}}\left[\Pi\left(\hat{\boldsymbol{\phi}}^{(\alpha)},\tilde{\boldsymbol{\phi}}^{(\alpha)},\boldsymbol{\lambda}\right)\right]\cdot\boldsymbol{\mu} \equiv R_{\lambda}\left(\boldsymbol{\mu},\hat{\boldsymbol{\phi}}^{(\alpha)},\tilde{\boldsymbol{\phi}}^{(\alpha)}\right) = -\int_{\Gamma_I}\boldsymbol{\mu}\cdot\left[\!\left[\tilde{\boldsymbol{\phi}}\circ\hat{\boldsymbol{\phi}}\right]\!\right]\mathrm{d}A = 0 \tag{24}$$

Fine-scale problem $\mathcal{F}$

$$\mathrm{D}_{\tilde{\boldsymbol{\phi}}^{(\alpha)}}\left[\Pi\left(\hat{\boldsymbol{\phi}}^{(\alpha)},\tilde{\boldsymbol{\phi}}^{(\alpha)},\boldsymbol{\lambda}\right)\right]\cdot\tilde{\boldsymbol{\eta}}_o^{(\alpha)} = R_{\phi}\left(\tilde{\boldsymbol{\eta}}_o^{(\alpha)};\hat{\boldsymbol{\phi}}^{(\alpha)},\tilde{\boldsymbol{\phi}}^{(\alpha)},\boldsymbol{\lambda}\right)$$
$$= \sum_{\alpha=1}^{2}\int_{\Omega^{(\alpha)}}\left[\mathrm{GRAD}\,\tilde{\boldsymbol{\eta}}_o^{(\alpha)}:\boldsymbol{P}^{(\alpha)} - \tilde{\boldsymbol{\eta}}_o^{(\alpha)}\cdot\rho_o^{(\alpha)}\boldsymbol{B}^{(\alpha)}\right]\mathrm{d}V \tag{25}$$
$$-\int_{\Gamma_I}\boldsymbol{\lambda}\cdot[\![\tilde{\boldsymbol{\eta}}_o]\!]\,\mathrm{d}A = 0$$

We would now like to adapt the fine-scale modeling procedure presented in [19] to convert the system (23)-(25) into a primal formulation in which $\hat{\boldsymbol{\phi}}^{(\alpha)}$ is the sole unknown. This objective is

achieved through a three-stage modeling process. First, the fine-scale Equation (25) is localized to the vicinity of the interface Γ_I and subsequently linearized to obtain a closed-form expression for $\tilde{\boldsymbol{\phi}}^{(\alpha)}$ in terms of $\hat{\boldsymbol{\phi}}^{(\alpha)}$ and $\boldsymbol{\lambda}$. Second, this fine-scale model is substituted into (24) to yield a point-wise expression for $\boldsymbol{\lambda}$ in terms of $\hat{\boldsymbol{\phi}}^{(\alpha)}$. Finally, these models for $\boldsymbol{\lambda}$ and $\tilde{\boldsymbol{\phi}}^{(\alpha)}$ are consistently embedded into (23) to remove their explicit appearance while retaining their effects.

Remark:

These derivations result in additional interface terms that have a form analogous to numerical flux and penalty terms found in standard Nitsche or DG formulations [5, 7, 9, 12]. However, the specific form of these terms is usually selected by the user based on the long history of the method, and multiple options have been proposed within the context of nonlinear solid mechanics [2, 10, 21, 26, 27, 43]. Herein, these terms arise naturally through the modeling of fine scales within a Lagrange multiplier interface formulation, thereby providing a rational basis for their origin.

3.1. Modeling of fine scales

The first modeling step is to localize the fine-scale problem (25) around the interface Γ_I. This is a reasonable assumption because the boundary layer effects are invariably localized in a narrow band around the interface and domain boundaries; in solid mechanics, this effect is known as Saint-Venant's principle. In the present problem, these effects are produced because of mesh nonconformity and the introduction of discrete Lagrange multipliers at the interface.

Accordingly, the effects of $\tilde{\boldsymbol{\phi}}^{(\alpha)}$ are assumed to vanish outside of a small neighborhood of the interface Γ_I. Herein, we adopt an explicit representation of the fine-scale fields according to the procedure described in [19], which we summarize herein for clarity. Recalling the finite element discretization of the regions $\Omega^{(1)}$ and $\Omega^{(2)}$, define a partition of the interface Γ_I into disjoint segments γ_s such that $\bigcup_{s=1}^{n_{seg}} \bar{\gamma}_s = \bar{\Gamma}_I$, where n_{seg} is the number of segments. Each segment is generated such that it is bordered by only a single element from each region $\Omega^{(\alpha)}$, namely $\gamma_s \subseteq \Gamma_{I,e}^{(\alpha)}$ for some element $\Omega_e^{(\alpha)}$ and $\gamma_s \cap \Gamma_{I,j}^{(\alpha)}$ for all $j \neq e$. Next, on both sides of segment γ_s, we associate a sector $\omega_s^{(\alpha)}$ that is a subset of the adjoining element $\Omega_e^{(\alpha)}$ such that one portion of the boundary $\partial\omega_s^{(\alpha)}$ corresponds with the segment: $\partial\omega_s^{(\alpha)} \cap \Gamma_I = \gamma_s$. An example partition is shown for a small interface in Figure 3; we also refer the reader to [19] for further elaboration on these definitions. Finally, we elect to represent the fine scales as edge bubble functions $b_s^{(\alpha)}$ spanning these sectors adjoining the interface:

$$\tilde{\boldsymbol{\phi}}^{(\alpha)}\Big|_{\omega_s^{(\alpha)}} = \boldsymbol{\beta}_s^{(\alpha)} b_s^{(\alpha)}(X), \qquad \tilde{\boldsymbol{\eta}}_o^{(\alpha)}\Big|_{\omega_s^{(\alpha)}} = \boldsymbol{\gamma}_s^{(\alpha)} b_s^{(\alpha)}(X) \qquad (26)$$

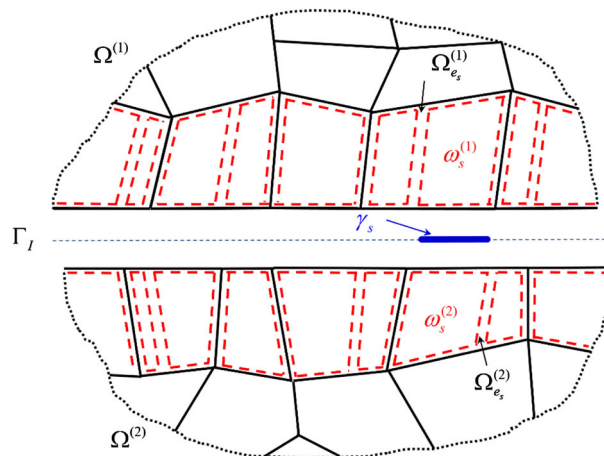Figure 3. Interface partition into segments γ_s and sectors $\omega_s^{(\alpha)}$.

where the bubble functions are nonzero on segment γ_s and vanish along the remainder of the sector boundary $\partial \omega_s^{(\alpha)}$.

As a result of the localized representation of the fine scales (26), the fine-scale problem (25) can be segregated into a series of local problems defined over pairs of sectors along the interface:

$$\tilde{R}_s \left(\hat{\boldsymbol{\eta}}_o^{(\alpha)}; \hat{\boldsymbol{\phi}}^{(\alpha)}, \tilde{\boldsymbol{\phi}}^{(\alpha)}, \boldsymbol{\lambda} \right) = \sum_{\alpha=1}^{2} \int_{\omega_s^{(\alpha)}} \left[\mathrm{GRAD}\, \tilde{\boldsymbol{\eta}}_o^{(\alpha)} : \boldsymbol{P}^{(\alpha)} - \tilde{\boldsymbol{\eta}}_o^{(\alpha)} \cdot \rho_o^{(\alpha)} \boldsymbol{B}^{(\alpha)} \right] \mathrm{d}V$$
$$- \int_{\gamma_s} \boldsymbol{\lambda} \cdot [\![\tilde{\boldsymbol{\eta}}_o]\!] \, \mathrm{d}A = 0 \text{ for } s = 1, \ldots, n_{seg} \tag{27}$$

The next important step to enable a closed-form solution of the fine-scale problem (27) is to perform linearization along the lines of [35]. Because the fine-scale field has been localized, the effects of this further modeling approximation are also confined to the interface. Thus, fine scales are treated as an incremental displacement $\Delta \tilde{\boldsymbol{u}}^{(\alpha)}$ about the coarse-scale deformation $\hat{\boldsymbol{\phi}}^{(\alpha)}$:

$$\sum_{\alpha=1}^{2} \int_{\Omega^{(\alpha)}} \mathrm{GRAD}\, \tilde{\boldsymbol{\eta}}_o^{(\alpha)} : \mathbf{A}^{(\alpha)} \left(\boldsymbol{F}^{(\alpha)} \right) : \mathrm{GRAD}\, \Delta \tilde{\boldsymbol{u}}^{(\alpha)} \mathrm{d}V = -\tilde{R}_s \left(\hat{\boldsymbol{\eta}}_o^{(\alpha)}; \hat{\boldsymbol{\phi}}^{(\alpha)}, \mathbf{0}, \boldsymbol{\lambda} \right) \tag{28}$$

where the acoustic tensor of material moduli $\mathbf{A}^{(\alpha)} \left(\boldsymbol{F}^{(\alpha)} \right)$ is defined as follows:

$$\mathbf{A}^{(\alpha)} \left(\boldsymbol{F}^{(\alpha)} \right) = \frac{\partial^2 W^{(\alpha)}}{\partial \boldsymbol{F} \partial \boldsymbol{F}} \tag{29}$$

Because of this incremental approximation, the fine scales do not contribute significantly to the deformation gradient such that

$$\boldsymbol{F}^{(\alpha)} = (\boldsymbol{I} + \boldsymbol{0}) \cdot \hat{\boldsymbol{F}}^{(\alpha)} = \hat{\boldsymbol{F}}^{(\alpha)} \tag{30}$$

Remark:
In [35], the linearized fine-scale problem was expressed in terms of the second Piola–Kirchhoff stress tensor $\boldsymbol{S} = \frac{\partial W}{\partial \boldsymbol{E}}$ and the material tangent tensor $\mathbf{C} = \frac{\partial^2 W}{\partial \boldsymbol{E}^2}$, where $\boldsymbol{E}$ is the Green–Lagrange strain tensor. While that presentation makes explicit the effects of geometric and material nonlinearity, herein, we have employed derivations in terms of $\mathbf{A}$ to yield more compact expressions. There is a one-to-one correspondence between these tensors, presented, for example, in [29, 44] as well as in Appendix A.

Next, we substitute the explicit form of the fine scales (26) into (28), replacing $\boldsymbol{\beta}_s^{(\alpha)}$ by $\Delta \boldsymbol{\beta}_s^{(\alpha)}$, to obtain

$$\sum_{\alpha=1}^{2} \boldsymbol{\gamma}_s^{(\alpha)} \cdot \left[\int_{\omega_s^{(\alpha)}} \mathrm{GRAD}\, \boldsymbol{b}_s^{(\alpha)} : \mathbf{A}^{(\alpha)} : \mathrm{GRAD}\, \boldsymbol{b}_s^{(\alpha)} \mathrm{d}V \right] \cdot \Delta \boldsymbol{\beta}_s^{(\alpha)}$$
$$= \sum_{\alpha=1}^{2} \boldsymbol{\gamma}_s^{(\alpha)} \cdot \left[\int_{\omega_s^{(\alpha)}} \boldsymbol{b}_s^{(\alpha)} \cdot \left(\mathrm{DIV}\, \boldsymbol{P}^{(\alpha)} + \rho_o^{(\alpha)} \boldsymbol{B}^{(\alpha)} \right) \mathrm{d}V \right]$$
$$+ \boldsymbol{\gamma}_s^{(1)} \cdot \left[\int_{\gamma_s} \boldsymbol{b}_s^{(1)} \cdot \left(-\boldsymbol{\lambda} - \boldsymbol{P}^{(1)} \cdot \boldsymbol{N}^{(1)} \right) \mathrm{d}A \right] + \boldsymbol{\gamma}_s^{(2)} \cdot \left[\int_{\gamma_s} \boldsymbol{b}_s^{(2)} \cdot \left(\boldsymbol{\lambda} - \boldsymbol{P}^{(2)} \cdot \boldsymbol{N}^{(2)} \right) \mathrm{d}A \right] \tag{31}$$

where $\boldsymbol{b}_s^{(\alpha)} = \sum_{J=1}^{n_{sd}} b_s^{(\alpha)} \boldsymbol{E}_J$ is a vector-valued bubble function and $\boldsymbol{E}_J$ are the basis vectors in the reference configuration. Note that integration by parts has been applied to the coarse-scale stress terms and the terms involving $\boldsymbol{\lambda}$ have been separated using the linearity of the jump operator.

Solving for the fine-scale coefficients $\Delta\boldsymbol{\beta}_s^{(\alpha)}$ in terms of the coarse-scale fields $\hat{\boldsymbol{\phi}}^{(\alpha)}$ and $\boldsymbol{\lambda}$ yields the following expression:

$$\Delta\boldsymbol{\beta}_s^{(\alpha)} = \tilde{\boldsymbol{\tau}}_s^{(\alpha)}\left[\int_{\omega_s^{(\alpha)}} \boldsymbol{b}_s^{(\alpha)}\cdot\left(\text{DIV }\boldsymbol{P}^{(\alpha)} + \rho_o^{(\alpha)}\boldsymbol{B}^{(\alpha)}\right)\text{d}V + \int_{\gamma_s} \boldsymbol{b}_s^{(\alpha)}\cdot\left[(-1)^{\alpha-1}\boldsymbol{\lambda} - \boldsymbol{P}^{(\alpha)}\cdot\boldsymbol{N}^{(\alpha)}\right]\text{d}A\right]$$
(32)

where the stability tensor $\tilde{\boldsymbol{\tau}}^{(\alpha)}$ is expressed in terms of the fine-scale bubble function and the material tangent tensor as follows:

$$\tilde{\boldsymbol{\tau}}_s^{(\alpha)} = \left[\int_{\omega_s^{(\alpha)}} \text{GRAD }\boldsymbol{b}_s^{(\alpha)} : \mathbf{A}^{(\alpha)} : \text{GRAD }\boldsymbol{b}_s^{(\alpha)}\text{d}V\right]^{-1}$$
(33)

We observe that the fine scales are driven by the residual of the equilibrium equation (2) and traction balance equation (5) incorporating the multiplier field $\boldsymbol{\lambda}$.

Three additional simplifying assumptions are now applied to further simplify (32) with direct analogy to [19]. First, the interior residual term is neglected, which is equivalent to assuming that the fine-scale bubble function is orthogonal to the coarse-scale residual, such as those employed by residual-free bubble methods [17, 45]. While this orthogonality condition will not be strictly enforced, larger contributions to the fine-scale model are expected from the boundary term. Second, the mean-value theorem is applied to extract the traction boundary residual outside of the integral, which converts (32) from a nonlocal to a local expression in terms of $\hat{\boldsymbol{u}}^{(\alpha)}$ and $\boldsymbol{\lambda}$. This step is a commonly employed technique in stabilized methods [37, 40]. Third, the average value of the bubble function is employed in expression (26) for $\tilde{\boldsymbol{\phi}}^{(\alpha)}$. Applying these modeling assumptions to (32) leads to an expression for $\Delta\tilde{\boldsymbol{u}}^{(\alpha)}$ that is analogous to stabilized methods:

$$\Delta\tilde{\boldsymbol{u}}^{(\alpha)} = \boldsymbol{\tau}_s^{(\alpha)}\cdot\left[(-1)^{\alpha-1}\boldsymbol{\lambda} - \boldsymbol{P}^{(\alpha)}\cdot\boldsymbol{N}^{(\alpha)}\right]$$
(34)

where

$$\boldsymbol{\tau}_s^{(\alpha)} = [\text{meas}(\gamma_s)]^{-1}\left(\int_{\gamma_s} b_s^{(\alpha)}\text{d}A\right)^2 \tilde{\boldsymbol{\tau}}_s^{(\alpha)}$$
(35)

Remark:
The definition for the stability tensor $\boldsymbol{\tau}_s^{(\alpha)}$ accounts for the interface-local finite element length scale through the dependence of the integrals on the segment γ_s, sector $\omega_s^{(\alpha)}$, and fine-scale bubble function $b_s^{(\alpha)}$. Also, the effects of evolving geometric and material nonlinearity on either side of the interface are encapsulated through the appearance of the acoustic tensor $\mathbf{A}^{(\alpha)}$. These dependencies will play a key role in the properties of the numerical flux and penalty parameter derived in the following section.

3.2. Variational embedding in the coarse-scale problem

The analytical model for the fine scales at the interface (34) will now be incorporated into the coarse-scale problem. We first concentrate on the contributions to the continuity equation (24) in order to obtain an expression for the Lagrange multiplier field $\boldsymbol{\lambda}$ and subsequently return to the equilibrium equation. This equation is nonlinear in $\boldsymbol{\phi}^{(\alpha)}$ because of the multiscale decomposition (13). Therefore, we linearize the jump operator as $[\![\tilde{\boldsymbol{\phi}}\circ\hat{\boldsymbol{\phi}}]\!] \simeq [\![\hat{\boldsymbol{\phi}}]\!] + [\![\Delta\tilde{\boldsymbol{u}}]\!]$, which is a valid approximation when the fine scales are small and localized as in the preceding section. Incorporating this result and expression (34) for the fine-scale increment $\Delta\boldsymbol{u}^{(\alpha)}$ into (24) leads to the following:

$$-\int_{\Gamma_I} \boldsymbol{\mu}\cdot\left[[\![\hat{\boldsymbol{\phi}}]\!] - \boldsymbol{\tau}_s^{(1)}\cdot\left(\boldsymbol{\lambda} - \boldsymbol{P}^{(1)}\cdot\boldsymbol{N}^{(1)}\right) + \boldsymbol{\tau}_s^{(2)}\cdot\left(-\boldsymbol{\lambda} - \boldsymbol{P}^{(2)}\cdot\boldsymbol{N}^{(2)}\right)\right]\text{d}A = 0$$
(36)

Next, proceeding according to [19], we employ a piecewise L^2 functional form for the Lagrange multipliers $\boldsymbol{\lambda}$ and $\boldsymbol{\mu}$, which is admissible because of the enhanced stability afforded by the fine-scale model. By requiring that (36) holds for all variations $\boldsymbol{\mu}$, the quantity in square brackets must vanish almost everywhere, in the notion of the L^2 projection. Therefore, the following expression must hold point-wise on each segment:

$$\boldsymbol{\tau}_s^{(1)} \cdot \boldsymbol{\lambda} + \boldsymbol{\tau}_s^{(2)} \cdot \boldsymbol{\lambda} = \boldsymbol{\tau}_s^{(1)} \cdot \boldsymbol{P}^{(1)} \cdot \boldsymbol{N}^{(1)} - \boldsymbol{\tau}_s^{(2)} \cdot \boldsymbol{P}^{(2)} \cdot \boldsymbol{N}^{(2)} - \left[\!\left[\hat{\boldsymbol{\phi}} \right]\!\right] \quad \text{for } s = 1, \ldots, n_{seg} \quad (37)$$

where we have segregated the coarse-scale displacement terms from the multiplier terms. Solving this expression for $\boldsymbol{\lambda}$, we obtain

$$\boldsymbol{\lambda} = \left[\boldsymbol{\delta}_s^{(1)} \cdot \boldsymbol{P}^{(1)} \cdot \boldsymbol{N}^{(1)} - \boldsymbol{\delta}_s^{(2)} \cdot \boldsymbol{P}^{(2)} \cdot \boldsymbol{N}^{(2)} \right] - \boldsymbol{\tau}_s \cdot \left[\!\left[\hat{\boldsymbol{\phi}} \right]\!\right] \quad (38)$$

The flux weighting tensors $\boldsymbol{\delta}_s^{(\alpha)}$ and stability tensor $\boldsymbol{\tau}_s$ are defined in terms of $\boldsymbol{\tau}_s^{(\alpha)}$ with direct analogy to [19]:

$$\boldsymbol{\tau}_s = \left(\boldsymbol{\tau}_s^{(1)} + \boldsymbol{\tau}_s^{(2)} \right)^{-1}, \qquad \boldsymbol{\delta}_s^{(\alpha)} = \boldsymbol{\tau}_s \cdot \boldsymbol{\tau}_s^{(\alpha)} \quad (39)$$

With this explicit form for $\boldsymbol{\lambda}$, a simplified expression for the fine scales results from substitution in (34):

$$\Delta \tilde{\boldsymbol{u}}^{(1)} = -\boldsymbol{\delta}_s \left[\boldsymbol{P}^{(1)} \cdot \boldsymbol{N}^{(1)} + \boldsymbol{P}^{(2)} \cdot \boldsymbol{N}^{(2)} \right] - \boldsymbol{\delta}_s^{(1)T} \cdot \left[\!\left[\hat{\boldsymbol{\phi}} \right]\!\right] \quad (40)$$

$$\Delta \tilde{\boldsymbol{u}}^{(2)} = -\boldsymbol{\delta}_s \left[\boldsymbol{P}^{(1)} \cdot \boldsymbol{N}^{(1)} + \boldsymbol{P}^{(2)} \cdot \boldsymbol{N}^{(2)} \right] + \boldsymbol{\delta}_s^{(2)T} \cdot \left[\!\left[\hat{\boldsymbol{\phi}} \right]\!\right] \quad (41)$$

where we have employed the symmetry of the tensors $\boldsymbol{\tau}_s^{(\alpha)}$ and $\boldsymbol{\tau}_s$ (derived from (33)) to enable the substitution $\boldsymbol{\delta}_s^{(\alpha)T} = \boldsymbol{\tau}_s^{(\alpha)} \cdot \boldsymbol{\tau}_s$. Also, the additional stability tensor $\boldsymbol{\delta}_s$ arises during the substitution and is defined as follows:

$$\boldsymbol{\delta}_s = \boldsymbol{\tau}_s^{(1)} \cdot \boldsymbol{\delta}_s^{(2)} = \boldsymbol{\tau}_s^{(2)} \cdot \boldsymbol{\delta}_s^{(1)} = \left[\left(\boldsymbol{\tau}_s^{(1)} \right)^{-1} + \left(\boldsymbol{\tau}_s^{(2)} \right)^{-1} \right]^{-1} \quad (42)$$

Remark:
Note that in general $\boldsymbol{\delta}_s^{(\alpha)T} \neq \boldsymbol{\delta}_s^{(\alpha)}$ according to (39). Therefore, proper care must be taken during the following derivations and subsequent implementation to maintain the consistency and variational structure of the method.

We return to the weak form (23) and embed the representation of the fine scales (40)-(41) and the multiplier $\boldsymbol{\lambda}$ (38) to obtain a formulation that is only a function of the coarse scale $\hat{\boldsymbol{\phi}}^{(\alpha)}$. First, the stress term is linearized with respect to the fine scales:

$$\mathrm{D}_{\tilde{\phi}}^{(\alpha)} \left[\int_{\Omega^{(\alpha)}} \mathrm{GRAD}\, \hat{\boldsymbol{\eta}}_o^{(\alpha)} : \boldsymbol{P}^{(\alpha)} \mathrm{d}V \right] \cdot \Delta \tilde{\boldsymbol{u}}^{(\alpha)} = \int_{\Omega^{(\alpha)}} \mathrm{GRAD}\, \hat{\boldsymbol{\eta}}_o^{(\alpha)} : \mathbf{A}^{(\alpha)} : \mathrm{GRAD}\, \Delta \tilde{\boldsymbol{u}}^{(\alpha)} \mathrm{d}V \quad (43)$$

Next, we integrate this term by parts, taking into account the representation for the fine scales (26) that vanish on element boundaries that do not intersect the interface:

$$\int_{\Omega^{(\alpha)}} \mathrm{GRAD}\, \hat{\boldsymbol{\eta}}_o^{(\alpha)} : \mathbf{A}^{(\alpha)} : \mathrm{GRAD}\, \Delta \tilde{\boldsymbol{u}}^{(\alpha)} \mathrm{d}V = -\int_{\Omega^{(\alpha)}} \mathrm{DIV}\left[\mathrm{GRAD}\, \hat{\boldsymbol{\eta}}_o^{(\alpha)} : \mathbf{A}^{(\alpha)} \right] \cdot \Delta \tilde{\boldsymbol{u}}^{(\alpha)} \mathrm{d}V$$

$$+ \int_{\Gamma_I} \left[\left(\mathrm{GRAD}\, \hat{\boldsymbol{\eta}}_o^{(\alpha)} : \mathbf{A}^{(\alpha)} \right) \cdot \boldsymbol{N}^{(\alpha)} \right] \cdot \Delta \tilde{\boldsymbol{u}}^{(\alpha)} \mathrm{d}A$$

$$(44)$$

As was adopted in [19], we neglect the contribution of the domain interior term from the right-hand side of (44) to align with our assumption in Section 3.1 that the fine scales become vanishingly small with distance from the interface. Also, this assumption simplifies the final form of the method and enables the direct substitution of the interface fine-scale model (34). Incorporating the expressions for $\boldsymbol{\lambda}$ (38) and the fine-scale fields $\Delta \tilde{\boldsymbol{u}}^{(\alpha)}$ (40)-(41) along with (44) into the coarse-scale problem (23) yields the following stabilized interface formulation for finite deformations:

$$
\begin{aligned}
\sum_{\alpha=1}^{2} \int_{\Omega^{(\alpha)}} & \left[\text{GRAD}\, \hat{\boldsymbol{\eta}}_o^{(\alpha)} : \boldsymbol{P}^{(\alpha)} - \hat{\boldsymbol{\eta}}_o^{(\alpha)} \cdot \rho_o^{(\alpha)} \boldsymbol{B}^{(\alpha)} \right] \mathrm{d}V \\
& - \int_{\Gamma_I} [\![\hat{\boldsymbol{\eta}}_o]\!] \cdot \left(\boldsymbol{\delta}_s^{(1)} \cdot \boldsymbol{P}^{(1)} \cdot \boldsymbol{N}^{(1)} - \boldsymbol{\delta}_s^{(2)} \cdot \boldsymbol{P}^{(2)} \cdot \boldsymbol{N}^{(2)} \right) \mathrm{d}A \\
& + \int_{\Gamma_I} [\![\hat{\boldsymbol{\eta}}_o]\!] \cdot \boldsymbol{\tau}_s \cdot [\![\hat{\boldsymbol{\phi}}]\!] \, \mathrm{d}A \\
& - \int_{\Gamma_I} \left[\left(\text{GRAD}\, \hat{\boldsymbol{\eta}}_o^{(1)} : \mathbf{A}^{(1)} \right) \cdot \boldsymbol{N}^{(1)} \right] \cdot \boldsymbol{\delta}_s^{(1)T} \cdot [\![\hat{\boldsymbol{\phi}}]\!] \, \mathrm{d}A \\
& + \int_{\Gamma_I} \left[\left(\text{GRAD}\, \hat{\boldsymbol{\eta}}_o^{(2)} : \mathbf{A}^{(2)} \right) \cdot \boldsymbol{N}^{(2)} \right] \cdot \boldsymbol{\delta}_s^{(2)T} \cdot [\![\hat{\boldsymbol{\phi}}]\!] \, \mathrm{d}A \\
& - \int_{\Gamma_I} \left[\left(\text{GRAD}\, \hat{\boldsymbol{\eta}}_o^{(1)} : \mathbf{A}^{(1)} \right) \cdot \boldsymbol{N}^{(1)} \right] \cdot \boldsymbol{\delta}_s \left[\boldsymbol{P}^{(1)} \cdot \boldsymbol{N}^{(1)} + \boldsymbol{P}^{(2)} \cdot \boldsymbol{N}^{(2)} \right] \mathrm{d}A \\
& - \int_{\Gamma_I} \left[\left(\text{GRAD}\, \hat{\boldsymbol{\eta}}_o^{(2)} : \mathbf{A}^{(2)} \right) \cdot \boldsymbol{N}^{(2)} \right] \cdot \boldsymbol{\delta}_s \left[\boldsymbol{P}^{(1)} \cdot \boldsymbol{N}^{(1)} + \boldsymbol{P}^{(2)} \cdot \boldsymbol{N}^{(2)} \right] \mathrm{d}A = 0
\end{aligned}
\tag{45}
$$

To cast (45) in a more compact form, we introduce the following notation for the so-called weighted average flux operators:

$$
\{\boldsymbol{P} \cdot \boldsymbol{N}\} = \boldsymbol{\delta}_s^{(1)} \cdot \boldsymbol{P}^{(1)} \cdot \boldsymbol{N}^{(1)} - \boldsymbol{\delta}_s^{(2)} \cdot \boldsymbol{P}^{(2)} \cdot \boldsymbol{N}^{(2)}
\tag{46}
$$

$$
\begin{aligned}
\{(\text{GRAD}\, \hat{\boldsymbol{\eta}}_o : \mathbf{A}) \cdot \boldsymbol{N}\} = \ & \boldsymbol{\delta}_s^{(1)} \cdot \left[\left(\text{GRAD}\, \hat{\boldsymbol{\eta}}_o^{(1)} : \mathbf{A}^{(1)} \right) \cdot \boldsymbol{N}^{(1)} \right] \\
& - \boldsymbol{\delta}_s^{(2)} \cdot \left[\left(\text{GRAD}\, \hat{\boldsymbol{\eta}}_o^{(2)} : \mathbf{A}^{(2)} \right) \cdot \boldsymbol{N}^{(2)} \right]
\end{aligned}
\tag{47}
$$

Also, herein, we choose to neglect the contribution from the stress jump term, which is the last two terms in (45), in order to improve the computational expediency of the method. Namely, fewer terms would need to be calculated for the residual force vector and stiffness matrix, as discussed in Section 3.3. Also, this term and its counterpart in the small strain context [19] are not commonly employed in interface methods (see e.g., [4, 5, 12, 26, 27]). However, these terms may provide additional stability in the presence of highly nonlinear material response. Adopting these conventions in (45) and removing the superimposed hats for clarity, we arrive at the final form of the stabilized finite strain interface formulation:

$$
\begin{aligned}
R\left(\boldsymbol{\eta}_o^{(\alpha)}, \boldsymbol{\phi}^{(\alpha)} \right) = \ & \sum_{\alpha=1}^{2} \int_{\Omega^{(\alpha)}} \left[\text{GRAD}\, \boldsymbol{\eta}_o^{(\alpha)} : \boldsymbol{P}^{(\alpha)} - \boldsymbol{\eta}_o^{(\alpha)} \cdot \rho_o^{(\alpha)} \boldsymbol{B}^{(\alpha)} \right] \mathrm{d}V \\
& - \int_{\Gamma_I} [\![\boldsymbol{\eta}_o]\!] \cdot \{\boldsymbol{P} \cdot \boldsymbol{N}\} \, \mathrm{d}A - \int_{\Gamma_I} \{(\text{GRAD}\, \boldsymbol{\eta}_o : \mathbf{A}) \cdot \boldsymbol{N}\} \cdot [\![\boldsymbol{\phi}]\!] \, \mathrm{d}A \\
& + \int_{\Gamma_I} [\![\boldsymbol{\eta}_o]\!] \cdot \boldsymbol{\tau}_s \cdot [\![\boldsymbol{\phi}]\!] \, \mathrm{d}A = 0
\end{aligned}
\tag{48}
$$

A remarkable similarity is apparent between the formulation (48) and both linear [5, 9, 12] and nonlinear [2, 10, 24, 25, 27] DG and Nitsche interface methods. However, the key distinction is that the definitions for the numerical flux (46)-(47) and the penalty parameter (39) are derived with recourse to the modeling of fine scales to stabilize a Lagrange multiplier interface formulation. In particular, (48) is free from user-defined parameters. Because of the close analogy of the present derivations to those in the linear context [19], many of the salient features from that method carry over to the proposed formulation (48). For example, the definition for the flux weighting tensors delta exhibits the features of area-weighting approaches [16] and stiffness-weighting approaches [5]. The reader is referred to Section 2.3.2 of [19] for additional remarks.

Remark:

We emphasize the key feature unique to the present nonlinear context whereby the penalty tensor $\boldsymbol{\tau}_s$ evolves with the nonlinear deformations according to the stability tensors $\boldsymbol{\tau}_s^{(\alpha)}$. The evolution of these parameters leads to a robust formulation for highly nonlinear problems.

Remark:

The provision for the evolution of these stability parameters as a function of the evolving nonlinear fields is similar to the adaptive schemes proposed in [20, 27]. In the former, a heuristic approach wherein the penalty term is scaled locally by the minimum eigenvalue of the acoustic tensor is advocated based on a mathematical analysis of linearized stress-free elasticity. Rigorous bounds on stability are proved in the latter for a DG method containing nonstandard stabilizing terms that are valid for general nonlinear hyperelastic material response. In both cases, the numerical flux is defined through lifting operators and employs the simple average of the fields across the interface. Our derivation presented in this paper instead adopts the VMS philosophy for developing stabilized methods along the lines of [19, 35].

3.3. Consistent linearization

To complete the derivation in the preceding sections, we carry out the consistent linearization of the stabilized interface formulation (48) to provide the tangent stiffness matrix required for the Newton–Raphson nonlinear solution scheme. These derivations also highlight that the variational structure of the formulation, which originated from (19), has been preserved through the consistent fine-scale modeling procedure and condensation of the multiplier fields. Throughout, we will neglect the dependence of $\boldsymbol{\tau}_s$ and $\boldsymbol{\delta}_s^{(\alpha)}$ on the displacement field.

Because the penalty term is linear in the deformation fields $\boldsymbol{\phi}^{(\alpha)}$ and the treatment of the domain terms can be found elsewhere (see e.g., [29]), we focus on the contributions emanating from the interface flux terms. These contributions are highlighted in the following expression:

$$
\begin{aligned}
K\left(\boldsymbol{\eta}_o^{(\alpha)}, \Delta \boldsymbol{u}^{(\alpha)}; \boldsymbol{\phi}^{(\alpha)}\right) &= \mathrm{D}_{\boldsymbol{\phi}^{(\alpha)}}\left[R\left(\boldsymbol{\eta}_o^{(\alpha)}, \boldsymbol{\phi}^{(\alpha)}\right)\right] \cdot \Delta \boldsymbol{u}^{(\alpha)} \\
&= \sum_{\alpha=1}^{2} \int_{\Omega^{(\alpha)}} \mathrm{GRAD}\, \boldsymbol{\eta}_o^{(\alpha)} : \mathbf{A}^{(\alpha)} : \mathrm{GRAD}\, \Delta \boldsymbol{u}^{(\alpha)} \mathrm{d}V \\
&+ \sum_{\alpha=1}^{2} \int_{\Gamma_I} [\![\boldsymbol{\eta}_o]\!] \cdot \boldsymbol{\tau}_s \cdot \mathrm{D}_{\boldsymbol{\phi}^{(\alpha)}}\, [\![\boldsymbol{\phi}]\!] \cdot \Delta \boldsymbol{u}^{(\alpha)} \mathrm{d}A \\
&- \sum_{\alpha=1}^{2} \int_{\Gamma_I} [\![\boldsymbol{\eta}_o]\!] \cdot \mathrm{D}_{\boldsymbol{\phi}^{(\alpha)}}\, [\{\boldsymbol{P} \cdot \boldsymbol{N}\}] \cdot \Delta \boldsymbol{u}^{(\alpha)} \mathrm{d}A \\
&- \sum_{\alpha=1}^{2} \int_{\Gamma_I} \{(\mathrm{GRAD}\, \boldsymbol{\eta}_o : \mathbf{A}) \cdot \boldsymbol{N}\} \cdot \mathrm{D}_{\boldsymbol{\phi}^{(\alpha)}}\, [\![\boldsymbol{\phi}]\!] \cdot \Delta \boldsymbol{u}^{(\alpha)} \mathrm{d}A \\
&- \sum_{\alpha=1}^{2} \int_{\Gamma_I} \left\{\left(\mathrm{GRAD}\, \boldsymbol{\eta}_o : \left(\mathrm{D}_{\boldsymbol{\phi}^{(\alpha)}}[\mathbf{A}] \cdot \Delta \boldsymbol{u}^{(\alpha)}\right)\right) \cdot \boldsymbol{N}\right\} \cdot [\![\boldsymbol{\phi}]\!] \, \mathrm{d}A
\end{aligned}
\tag{49}
$$

The first interface term in (49) involving the first Piola–Kirchhoff stress follows similarly to the linearization of the fine-scale field presented in (43) by treating each component of the flux separately:

$$\sum_{\alpha=1}^{2} \mathrm{D}_{\phi^{(\alpha)}} \left[\{ \boldsymbol{P} \cdot \boldsymbol{N} \} \right] \cdot \Delta \boldsymbol{u}^{(\alpha)} = \delta_s^{(1)} \cdot \left(\mathrm{D}_{\phi^{(1)}} \left[\boldsymbol{P}^{(1)} \right] \cdot \Delta \boldsymbol{u}^{(1)} \right) \cdot \boldsymbol{N}^{(1)} - \delta_s^{(2)} \cdot \left(\mathrm{D}_{\phi^{(2)}} \left[\boldsymbol{P}^{(2)} \right] \cdot \Delta \boldsymbol{u}^{(2)} \right) \cdot \boldsymbol{N}^{(2)}$$

$$= \{ (\mathbf{A} : \mathrm{GRAD} \Delta \boldsymbol{u}) \cdot \boldsymbol{N} \} \tag{50}$$

Also, the second flux term is obtained trivially along with the penalty term through the linearity of the jump operator:

$$\sum_{\alpha=1}^{2} \mathrm{D}_{\phi^{(\alpha)}} \left[[\![\boldsymbol{\phi}]\!] \right] \cdot \Delta \boldsymbol{u}^{(\alpha)} = \Delta \boldsymbol{u}^{(1)} - \Delta \boldsymbol{u}^{(2)} = [\![\Delta \boldsymbol{u}]\!] \tag{51}$$

However, the last term gives rise to a nonstandard contribution because of the dependence of the acoustic tensor $\mathbf{A}$ on the deformation gradient $\boldsymbol{F}$. The result, similar to the term appearing in the interface method of Mergheim *et al.* [10], is expressed as follows:

$$\mathrm{D}_{\phi^{(\alpha)}} \left[\mathbf{A}^{(\alpha)} \right] \cdot \Delta \boldsymbol{u}^{(\alpha)} = \boldsymbol{\Xi}^{(\alpha)} : \mathrm{GRAD} \, \Delta \boldsymbol{u}^{(\alpha)} \tag{52}$$

where $\boldsymbol{\Xi}^{(\alpha)} \left(\boldsymbol{F}^{(\alpha)} \right)$ is a sixth-order tensor of material moduli defined as follows:

$$\boldsymbol{\Xi}^{(\alpha)} \left(\boldsymbol{F}^{(\alpha)} \right) = \frac{\partial^3 W^{(\alpha)}}{\partial \boldsymbol{F} \, \partial \boldsymbol{F} \, \partial \boldsymbol{F}} \tag{53}$$

The contraction of the tensors in (52) is handled through the extension of the double-contraction operator : to higher-order tensors in a similar manner as presented in Section 3.2 of [35].

Substituting (50)-(53) into (49) leads to the final linearized form:

$$K \left(\boldsymbol{\eta}_o^{(\alpha)}, \Delta \boldsymbol{u}^{(\alpha)}; \boldsymbol{\phi}^{(\alpha)} \right) = \sum_{\alpha=1}^{2} \int_{\Omega^{(\alpha)}} \mathrm{GRAD} \, \boldsymbol{\eta}_o^{(\alpha)} : \mathbf{A}^{(\alpha)} : \mathrm{GRAD} \, \Delta \boldsymbol{u}^{(\alpha)} \mathrm{d}V$$

$$+ \int_{\Gamma_I} [\![\boldsymbol{\eta}_o]\!] \cdot \boldsymbol{\tau}_s \cdot [\![\Delta \boldsymbol{u}]\!] \, \mathrm{d}A - \int_{\Gamma_I} [\![\boldsymbol{\eta}_o]\!] \cdot \{ (\mathbf{A} : \mathrm{GRAD} \, \Delta \boldsymbol{u}) \cdot \boldsymbol{N} \} \, \mathrm{d}A$$

$$- \int_{\Gamma_I} \{ (\mathrm{GRAD} \, \boldsymbol{\eta}_o : \mathbf{A}) \cdot \boldsymbol{N} \} \cdot [\![\Delta \boldsymbol{u}]\!] \, \mathrm{d}A$$

$$- \int_{\Gamma_I} \{ (\mathrm{GRAD} \, \boldsymbol{\eta}_o : \boldsymbol{\Xi} : \mathrm{GRAD} \, \Delta \boldsymbol{u}) \cdot \boldsymbol{N} \} \cdot [\![\boldsymbol{\phi}]\!] \, \mathrm{d}A \tag{54}$$

We observe that (54) is symmetric with respect to the variations $\boldsymbol{\eta}_o^{(\alpha)}$ and the incremental displacement $\Delta \boldsymbol{u}^{(\alpha)}$. Therefore, the underlying variational structure associated with the mixed interface problem (12) has been preserved throughout the fine-scale modeling procedure. The fact that the stiffness matrix is symmetric also makes this formulation amenable for incorporation into standard pure-displacement finite element codes. Additionally, once an explicit form of the material model $W^{(\alpha)}$ is chosen for each region $\Omega^{(\alpha)}$, all of the terms in the weak form (48) and the incremental form (54) can be directly evaluated through the constitutive equations (6), (29), and (53).

Remark:
The higher-order derivatives involved in the definition of $\boldsymbol{\Xi}^{(\alpha)}$ may be difficult to derive and subsequently expensive to evaluate within an element subroutine for complex material models. However, the term involving this sixth-order material moduli tensor in (54) is driven by the interface

residual, namely the discrete interface gap $[\![\boldsymbol{\phi}]\!]$. When the value of this residual is small within a finite element simulation, the contribution from this term becomes less significant. Also, this term does not appear in (48), and thus, it only contributes to the stiffness matrix. The effect of neglecting these terms will be considered in future work.

Remark:
While the derivations in Section 3 have been carried out in the reference configuration, the resulting expressions may be pushed forward to the spatial configuration, which may be easier to implement in the finite element context. We provide the spatial counterpart of the significant equations in Appendix A.

4. EXTENSION TO MULTIPLE INTERFACES AND FULLY DISCONTINUOUS APPROXIMATIONS

The preceding derivations can be readily extended to domains containing multiple interfaces and ultimately lead to a formulation analogous to the classical DG interior penalty method. To expand upon this point, consider the weak form (7) involving the Lagrange multiplier at the interface Γ_I. We apply the integration by parts and the divergence theorem in each domain $\Omega^{(\alpha)}$ to obtain the Euler–Lagrange equations through the weighted-residual form:

$$
\begin{aligned}
&-\sum_{\alpha=1}^{2} \int_{\Omega^{(\alpha)}} \boldsymbol{\eta}_o^{(\alpha)} \cdot \left(\mathrm{DIV}\, \boldsymbol{P}^{(\alpha)} + \rho_o^{(\alpha)} \boldsymbol{B}^{(\alpha)} \right) \mathrm{d}V + \sum_{\alpha=1}^{2} \int_{\Gamma^{(\alpha)} \backslash \Gamma_I} \left(\boldsymbol{P}^{(\alpha)} \cdot \boldsymbol{N}^{(\alpha)} \right) \cdot \boldsymbol{\eta}_o^{(\alpha)} \mathrm{d}A \\
&+ \int_{\Gamma_I} \left(\boldsymbol{P}^{(1)} \cdot \boldsymbol{N}^{(1)} - \boldsymbol{\lambda} \right) \cdot \boldsymbol{\eta}_o^{(1)} \mathrm{d}A + \int_{\Gamma_I} \left(\boldsymbol{P}^{(2)} \cdot \boldsymbol{N}^{(2)} + \boldsymbol{\lambda} \right) \cdot \boldsymbol{\eta}_o^{(2)} \mathrm{d}A = 0
\end{aligned}
\tag{55}
$$

Here, the traction boundary integral $\partial \Omega^{(\alpha)} = \Gamma^{(\alpha)}$ has been split into a portion adjoining the interface and the remainder of the boundary. The terms on $\Gamma^{(\alpha)} \backslash \Gamma_I$ vanish because $\boldsymbol{\eta}_o^{(\alpha)} = \boldsymbol{0}$ according to the functional space $\mathcal{V}^{(\alpha)}$ in (10). Therefore, upon invoking the fundamental theorem of the calculus of variations, we arrive at the equilibrium equation in each region $\Omega^{(\alpha)}$ as in (2) along with traction equilibrium on Γ_I as in (5) imposed through $\boldsymbol{\lambda}$.

Now suppose that multiple interfaces are present in domain Ω. The continuity conditions on each interface can be imposed weakly by incorporating independent Lagrange multiplier fields $\boldsymbol{\lambda}^{(\beta)}$ over each unique pair of adjacent region boundaries. The corresponding weak form would be the generalization of the integrals in (5) to summations over all domain regions and over all region boundary pairs constituting interfaces. However, by assuming that the fine-scale fields are localized to the vicinity of the interfaces, the fine-scale problem corresponding to (25) may again be separated into a series of smaller problems posed over individual interfaces and, furthermore, over discrete interface segments as in (27). Thereafter, the remainder of the derivations applies identically to each specific interface, allowing a condensation of each $\boldsymbol{\lambda}^{(\beta)}$ analogous to (38) and resulting in a global problem expressed entirely in terms of the coarse scale $\hat{\boldsymbol{\phi}}^{(\alpha)}$ across all regions.

Taking this argument further, let the domain Ω be discretized into a set of finite elements $\{\Omega_e\}_{e=1}^{n_{umel}}$. Within the context of the preceding discussion, we now treat each inter-element boundary as an interface and each element as a region. By weakly imposing continuity across each pair of adjacent elements, we arrive at a fully discontinuous approximation of the solution field $\boldsymbol{\phi}$, where the integrals in (48) are evaluated over all element interiors $\tilde{\Omega}$ and element interfaces $\tilde{\Gamma}$. The resulting formulation appears quite similar to the classical interior penalty DG method [7, 10, 12, 24]. Note that in these methods, the numerical flux is almost invariably defined as the arithmetic average of tractions and the penalty parameter is obtained via dimensional and scaling arguments. In contrast, we emphasize that the penalty parameter contained herein has been consistently derived and the numerical flux is obtained as a weighted average according to (46).

Remark:

A strong point of the present framework is that it naturally accommodates a spectrum of problems from domains with a single interface to domains with multiple interfaces and to fully discontinuous approximations across finite element boundaries. The inherent stability enabling this range of problem classes derives from the stability afforded by the evolving fine-scale models for $\tau_s^{(\alpha)}$.

Remark:

As is the case among almost all DG methods, the fully discontinuous approximation case is computationally more expensive than the corresponding continuous Galerkin approximation for the same number of elements because of the increased number of degrees of freedom in the global stiffness matrix. This cost is greatly reduced for domains with specific nonconforming interfaces wherein continuous approximations are employed in the region interiors. For such problems, the cost of the present method is lower than the comparable mortar methods because the Lagrange multiplier field is not solved as an added unknown in the discrete problem. The only relative increase in element-level calculations compared with existing DG methods [24] and Nitsche methods [16] is the evaluation of the stability tensors, which represents the crucial benefit of the proposed method. A remark on the relative cost increase at the interface element level is contained in Section 6.3.

Remark:

Special care must be taken when localizing the fine scales within elements in the context of the fully discontinuous approximation. For example, consider a triangular element Ω_e that has individual interface segments $\gamma_s^{(\beta)}$ corresponding to each of its three edges. Each segment is assigned a sector $\omega_s^{(\beta)} \subseteq \Omega_e$ over which a portion of the fine-scale field $\tilde{\phi}$ is supported as in (26). Strictly speaking, to ensure that the fine-scale problems (27) for each interface segment/sector pair remain independent, the sectors $\omega_s^{(\beta)}$ within the common element Ω_e must not overlap, namely $\omega_s^{(1)} \cap \omega_s^{(2)} = \emptyset, \omega_s^{(2)} \cap \omega_s^{(3)} = \emptyset$, and $\omega_s^{(3)} \cap \omega_s^{(1)} = \emptyset$. This issue is discussed further in Section 5.

5. ASPECTS OF IMPLEMENTATION: FINE-SCALE SECTORS AND BUBBLE FUNCTIONS

In this section, we elaborate on the key aspects of our implementation of the proposed method. As noted in [19], the choice of the fine-scale bubble functions $b_s^{(\alpha)}$ has an important impact on the accuracy of the computed results. One possible representation considered in other interface methods [17] is the use of residual-free bubbles, which are designed to be orthogonal to the space of the coarse-scale equilibrium residual, implying $\int_{\omega_s^{(\alpha)}} b_s^{(\alpha)} \cdot \left(\text{DIV } P^{(\alpha)} + \rho_o^{(\alpha)} B^{(\alpha)} \right) dV = 0$. Although these functions satisfy the assumption that was employed to simplify the fine-scale solution (32), they are obtained by solving a local boundary-value problem and are therefore quite expensive. As an alternative, simple polynomial bubble functions were analyzed in [19] for two-dimensional linear elasticity problems and found to provide robust performance across various element types and mesh distortion. Therefore, we elect to use these edge bubble functions for the present nonlinear formulation, which are summarized in Table I; note that the letter and number designate the element shape and number of nodes, respectively. For three-dimensional domains, the authors proposed in [19] to partition the interface into triangular segments in order to accommodate general nonconforming meshes. The corresponding sectors for tetrahedral and hexahedral elements take the form of smaller tetrahedral and wedge-shaped regions, respectively. Polynomial bubble functions that are nonzero within the base of these sectors are listed in Table II. To simplify these tables, the reference sector coordinate system (ξ, η) or (ξ, η, ζ) is assumed to be oriented such that the interface segment corresponds to the bottom of the sector. The reader is referred to [19] for several figures illustrating the definitions of the sectors along with further discussion on the bubble functions.

Another key factor in the fine-scale modeling procedure is the definition of the interface sectors $\omega_s^{(\alpha)} \subseteq \Omega_e$ over which the localized fine-scale equation (27) is solved. An obvious convention is to define a tributary sector that extends from the interface segment through the entire depth of the

Table I. Edge bubble functions employed for fine-scale
fields, two dimensions.

Element	Bubble function
T3	$4\xi(1 - \xi - \eta)$
Q4	$\frac{1}{2}\left(1 - \xi^2\right)\left(1 - \eta\right)$
T6	$4\xi^2(1 - \xi - \eta)^2$
Q9	$\frac{1}{4}\left(1 - \xi^4\right)(1 - \eta)^2 + \frac{1}{4}\left(1 - \xi^2\right)(1 - \eta)$

Table II. Face bubble functions employed for
fine-scale fields, three dimensions.

Element	Bubble function
T4	$27\xi\eta(1 - \xi - \eta - \zeta)$
B8	$\frac{27}{2}\xi\eta(1 - \xi - \eta)(1 - \zeta)$

element, as illustrated in Figure 3. However, the authors advocated in [19] to employ truncated definitions of the interface sectors for elements with large aspect ratios, whereby the maximum extension of the sector into the element is approximately limited to the size of the segment γ_s. This procedure, contained in Boxes 1 to 4 of [19], is related solely to the element geometry in the reference configuration and readily extendable to the present nonlinear formulation. Therefore, we adopt it for the numerical studies in Section 6. Note that the integrals in the fine-scale model (27) are performed in the reference configuration; as such, we treat the image of the interface sectors in the reference configuration to be fixed throughout the course of the numerical simulations.

Remark:
A physical motivation for limiting the support of the bubble functions is that the interfacial effects, which they model, are localized according to Saint-Venant's principle, mentioned previously in Section 3.2. While other functions that decay exponentially with distance from the interface could be proposed, the bubble functions presented here have the advantages of being simple in form and easily integrated by numerical quadrature.

As remarked at the end of Section 4, instances may arise in which an element has multiple edges serving as interfaces, particularly in the case when fully discontinuous approximations are employed. Each of the sectors that are assigned to these edges should be taken as disjoint regions of the element such that the localized fine-scale problems (27) remain independent. A possible definition for the sectors of a quadrilateral element with all four edges identified as interface segments is illustrated in Figure 4. However, the definition of such regions is not directly compatible with the procedure summarized in the preceding paragraphs, which is adapted from [19]. Previously, the sectors were assumed to be freely extendable across the entire depth of the element in the direction orthogonal to the interface segment without conflict from neighboring sectors. In order to keep the implementation of the method simple, we adopt the following heuristic approach. For each edge serving as an interface segment, we define the sector according to the appropriate Box from [19] without considering the presence of other segments. Then, the value of the stabilizing tensor $\boldsymbol{\tau}_s^{(\alpha)}$ for each sector is computed using (35). Finally, each tensor is scaled down by the number of edges e_s : $\bar{\boldsymbol{\tau}}_s^{(\alpha)} = (e_s)^{-1}\boldsymbol{\tau}_s^{(\alpha)}$ to approximately account for the overlap of the sectors. For example, notice that in Figure 4, the area of each sector $\omega_s^{(\alpha)}$ is one-fourth the area of Ω_e. The values of $\bar{\boldsymbol{\tau}}_s^{(\alpha)} = (e_s)^{-1}\boldsymbol{\tau}_s^{(\alpha)}$ are then substituted into definition (39) for the numerical flux weights $\boldsymbol{\delta}_s^{(\alpha)}$
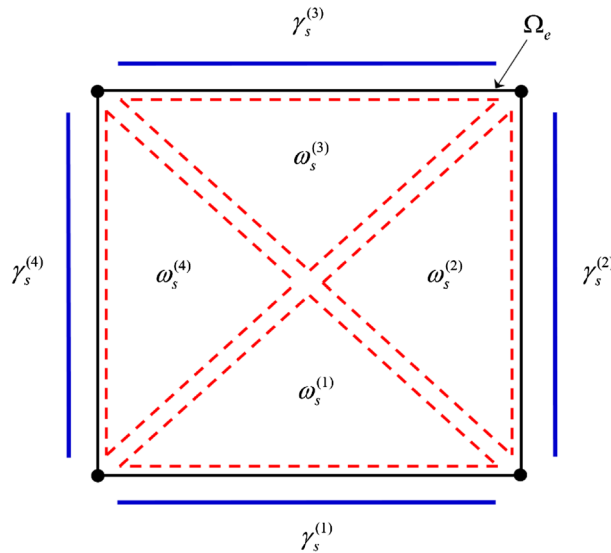
Figure 4. Disjoint sectors within a quadrilateral element possessing multiple interface segments.

and the penalty parameter τ_s. Combining the definitions of the bubble functions $b_s^{(\alpha)}$ from Tables I and II with the previous definitions for the sectors $\omega_s^{(\alpha)}$ completes the description of the fine-scale models employed in this study.

Remark:
Notice from definition (39) that when the stability tensors $\tau_s^{(1)} \approx \tau_s^{(2)}$ across a segment, the weights $\delta_s^{(\alpha)}$ are not significantly affected by this heuristic modification of $\tau_s^{(\alpha)}$. In contrast, the value of the stability parameter τ_s is increased proportional to e_s. This small increase tends to enhance the stability of the method without inducing ill conditioning of the stiffness matrix (54).

6. NUMERICAL RESULTS

We investigate the performance of the proposed interface method across a range of deformation modes. Standard Lagrange polynomials are employed within the finite elements of either linear or quadratic degree, and both two-dimensional and three-dimensional problems are considered. A common neo-Hookean material model is employed for each of the problems, with a strain energy density function as follows:

$$W(F) = \frac{1}{2}\mu \left(\text{tr}\left(F^T F \right) - 3 \right) - \mu \ln J + \frac{1}{2}\lambda (J - 1)^2 \tag{56}$$

Expressions for the corresponding constitutive tensors P, $\mathbf{A}$, and Ξ are provided in the Appendix. All integral expressions over surfaces and volumes are evaluated using Gauss quadrature rules of sufficient degree. Results are presented first for meshes with specific interfaces where continuity is weakly imposed, which corresponds with the formulation derived in Sections 2 and 3. Additional numerical tests are performed using fully discontinuous approximations across all elements as illustrations of the multiple interface formulation discussed in Section 4. To distinguish these cases, we refer to the former case by the name stabilized Nitsche interface method while the latter case is termed as the stabilized DG method.

Remark:
The integration of the material contribution to $\tau_s^{(\alpha)}$ according to (33) is performed over the interface sector $\omega_s^{(\alpha)}$, which is typically a subset of the element Ω_e. However, the acoustic tensor $\mathbf{A}^{(\alpha)}$ is evaluated in terms of the deformation gradient F, which is a function of the coarse-scale deformation
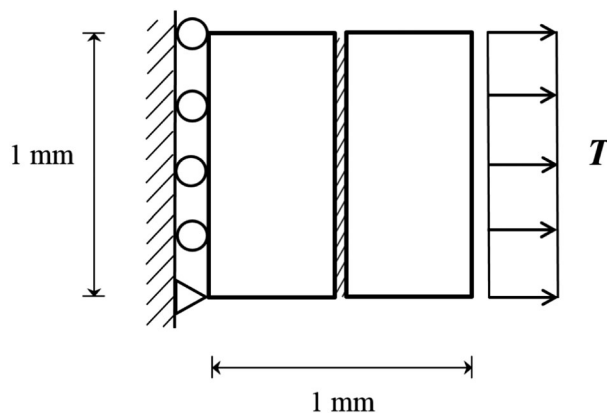
Figure 5. Patch test problem description.

$\hat{\boldsymbol{\phi}}$ defined over the entire element. Thus, evaluating these integrals requires a transformation of coordinates between the sector and the parent element, which is not encountered for homogeneous materials in the linear setting [19].

Remark:
Because the fine-scale tensors $\boldsymbol{\tau}_s^{(\alpha)}$ are a function of the deformation, their value evolves during each iteration of the Newton–Raphson solution procedure. However, this effect is not accounted for in the linearization provided in Section 3.3, as remarked at that point. Similar to observations in the context of a VMS formulation for nonlinear incompressible elasticity [35], neglecting these effects leads to a reduced convergence rate of the out-of-balance force vector. To restore the quadratic rate of iterative convergence, the value of $\boldsymbol{\tau}_s^{(\alpha)}$ can be frozen for each interface segment after a specified number of iterations and held constant over the remainder of the load step. Herein, the value is frozen after three iterations.

6.1. Tensile patch test

We begin by solving a simple patch test to verify the consistency of the interface formulation. A rectangular bar of 1 mm × 1 mm is separated into two rectangular regions by a nonconforming interface over which the proposed stabilized Nitsche interface method is employed, as shown in Figure 5. The material properties within the neo-Hookean model (56) are taken as $E = 100$ MPa and $\nu = 0.25$. A uniform traction of 20 MPa is applied to the right edge of the domain, and boundary conditions are assigned on the left face in order to create a state of uniform tensile stress throughout the specimen. Under these conditions, the exact value for the tip elongation is $\delta = 0.2110$.

Two meshes that contain linear triangular and quadrilateral elements, respectively, as shown in Figure 6, are considered. Each region contains four quadrilateral elements; the triangular mesh is obtained by bisecting the quadrilateral elements. In the left region, the elements are rectangles $0.25\times$ 0.5; in the right region, the line of nodes in the center is dropped downward to the coordinate $Y = 0.4$ to make the interface nonconforming. The traction field is applied in a single-load step to produce the numerical solutions in Figure 6. The solution field from both meshes is smooth and reproduces the exact value of the tip displacement, with the displacement gap between the regions correctly resolved as identically zero.

In Table III, we record the Euclidean norm of the out-of-balance force vector computed at each iteration during the Newton–Raphson solution procedure. The observed quadratic convergence rate numerically confirms the consistent linearization and tangent matrix provided in Section 3.3.

6.2. Trapezoidal deformation problem

As further verification of consistency and stability, we consider another problem with an exact solution that was originally proposed in [35]. The geometry consists of a square domain that
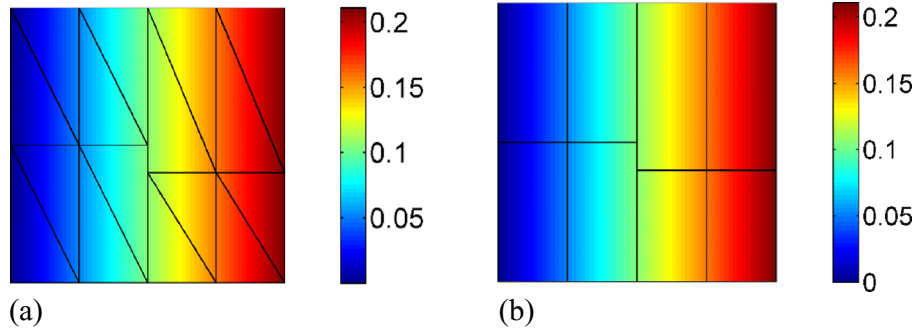
Figure 6. Displacement u_x contour on nonconforming meshes: (a) triangular mesh; (b) quadrilateral mesh.

Table III. Evolution of residual l^2 norm for nonconforming meshes.

Iteration number	Residual norm	
	T3 elements	Q4 elements
1	5.6094580×10^{-2}	5.6094580×10^{-2}
2	2.9576726×10^{-5}	2.9576726×10^{-5}
3	$8.1814644 \times 10^{-12}$	$8.1870099 \times 10^{-12}$
4	$3.0798871 \times 10^{-14}$	$2.2733456 \times 10^{-14}$
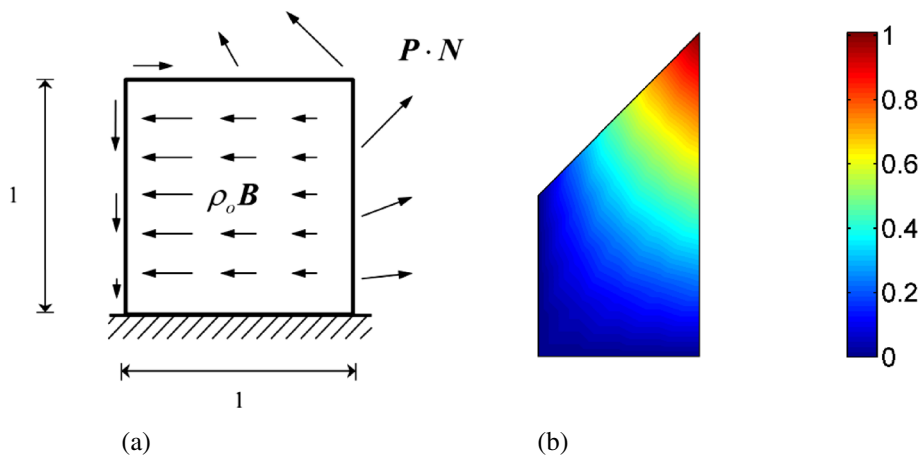
Figure 7. Trapezoidal deformation problem: (a) problem domain; (b) exact vertical displacement on deformed configuration.

is subsequently deformed into a trapezoid by raising the upper right-hand corner. A single pure-displacement quadrilateral element is capable of representing this deformation mode, as shown in Figure 7(b). The analytical solution is reproduced below in Cartesian coordinates in terms of the vertical displacement δ of the corner node:

$$x = X, \qquad y = \delta XY + Y, \qquad z = Z \tag{57}$$

The deformation gradient and Jacobian are given as follows:

$$\boldsymbol{F} = \begin{bmatrix} 1 & 0 & 0 \\ \delta Y & \delta X + 1 & 0 \\ 0 & 0 & 1 \end{bmatrix}, \qquad J = \delta X + 1 \tag{58}$$
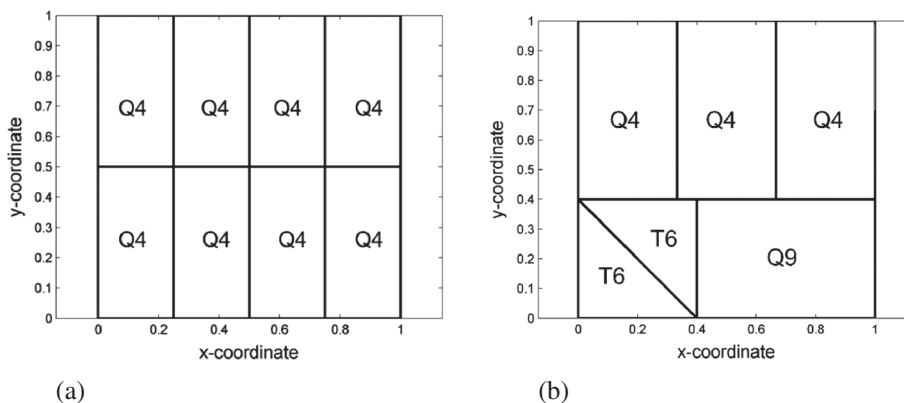
Figure 8. Nonconforming meshes: (a) bilinear quadrilaterals; (b) linear and quadratic elements.

Considering the stored elastic strain energy function given by (56), the first Piola–Kirchhoff stress tensor follows as

$$
\boldsymbol{P} = \begin{bmatrix} \delta\lambda J X & \delta\mu Y/J - \delta^2\lambda X Y & 0 \\ \delta\mu Y & [\delta X(\lambda J + \mu + \mu J)]/J & 0 \\ 0 & 0 & \delta\lambda J X \end{bmatrix}
\tag{59}
$$

Substituting (59) into (2) leads to an expression for the body force term (60):

$$
\rho_o \boldsymbol{B} = -\mathrm{DIV}\,\boldsymbol{P} = \begin{bmatrix} -(\delta\mu/J + \delta\lambda J) & 0 & 0 \end{bmatrix}^T
\tag{60}
$$

The material parameters are taken as $\lambda = \mu = 40$, and the load parameter as $\delta = 1.01$. To investigate this problem in the numerical setting, we apply fixed boundary conditions on the lower edge and apply the analytical tractions arising from (59) on the other edges, as depicted in Figure 7(a). Because of the appearance of $J = \delta X + 1$ in the denominator of (59) and (60), the integrands within the finite element residual vector and tangent matrix will contain rational polynomials that are not precisely evaluated through low-order Gauss quadrature. In order to obtain the exact solution to numerical precision, we employ higher-order rules using 10×10 quadrature points for element-interior integrals and 10 points for boundary or interface integrals.

Two discretizations of the domain are considered, as shown in Figure 8. The first mesh consists of two regions of four bilinear quadrilateral elements separated by an initially horizontal stabilized Nitsche interface. In the second mesh, the lower region is represented using two quadratic triangular elements in the lower left and one biquadratic element in the lower right; the upper region contains three bilinear quadrilaterals such that the interface is nonconforming. Note that linear triangular elements cannot reproduce the exact solution except in the limit of mesh refinement [35] and, thus, are not employed in this study. Also, the mid-side nodes of the quadratic elements must be located at the midpoint of the associated element edge in order for the finite element shape functions to reproduce the exact solution. Using this problem, we investigate the performance of the interface method for higher-order elements and for an interface that undergoes rotation during the loading.

The body force and tractions (59)-(60) are applied in four equal load steps to reach the deformed configurations presented in Figure 9. For both meshes, the displacement field matches precisely with the solution contour in Figure 7(b), confirming the consistency of the formulation. No gaps or distortion of the interface is evident in the discrete response. Thus, the proposed interface method is capable of tying meshes with different element types across interfaces undergoing finite deformations.

In Table IV, we again show the Euclidean norm of the out-of-balance force vector computed at each iteration during the Newton–Raphson solution procedure. The quadratic convergence rate is achieved.
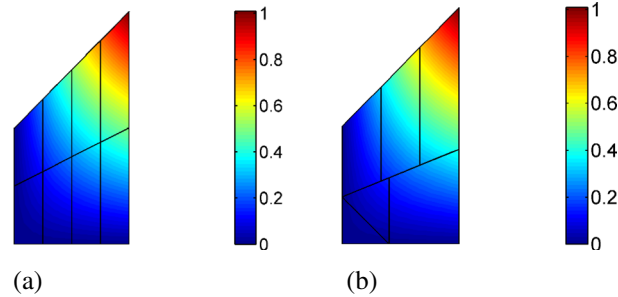
Figure 9. Vertical displacement contours on deformed configuration: (a) bilinear quadrilaterals; (b) mixture of linear and quadratic elements.

Table IV. Evolution of residual l^2 norm for two different mesh types.

Iteration number	Residual norm	
	Q4 elements	Q4-T6-Q9 elements
1	6.1686067×10^{-1}	1.0397659×10^{0}
2	2.6368099×10^{-2}	1.8790396×10^{-2}
3	2.0567903×10^{-6}	5.0704490×10^{-6}
4	$4.0519883 \times 10^{-14}$	$4.0763657 \times 10^{-13}$

Remark:
The number of quadrature points is increased solely for this numerical example in order to resolve the analytical solution to numerical precision. For low-order rules, the slight errors in the discrete solution are directly attributed to the quadrature error. Note that because the stress tensor (59) involves rational polynomials, the computation of the internal force vector associated with (48) also requires higher-order quadrature. As an alternative, quadrature rules for integrating rational functions could be employed.

6.3. Parabolic indentation of a square block

In this problem, we investigate the ability of the fine-scale models to provide varying levels of stabilization across a domain in accordance with the evolving geometric and material nonlinearity. The domain consists of a bi-unit square with fixed boundary conditions on the lower edge and traction-free vertical edges. The top surface of the block is indented by an applied displacement that maps it into a parabola according to the following:

$$u_2(X_1, X_2 = 1.0) = a(X_1 - 0.25)(X_1 - 0.75) \tag{61}$$

where a is a proportional loading parameter and the horizontal displacement component is left free. This problem was originally studied by Ten Eyck and Lew [27]; the distinguishing feature is that the acoustic tensor **A** becomes indefinite in the vicinity of the bowl of the parabola for values of $a > 0.1$. The resulting negative eigenvalues are an indicator of localized material instability. When a DG method with a spatially uniform value for the stabilization parameter was employed, spurious oscillations in the inter-element displacement field jumps were manifested in this region of the domain. This observation prompted the adaptive stabilization strategy in [27] where the stability parameter along each element edge was scaled by the magnitude of the largest negative eigenvalue of **A** along that same edge. This strategy led to stable discrete response whereby the jump discontinuities were controlled throughout the domain.

Presently, we employ a DG approximation using linear triangular elements within the interface method proposed herein. The key idea is to determine whether the consistent definitions for the numerical flux and penalty parameter (39) are able to naturally accommodate the local material

instability. Three levels of mesh resolution are selected to coincide with the meshes from [27]. However, the Dirichlet boundary conditions are strongly rather than weakly imposed, which leads to slight discrepancies in the computed results compared with the reference. The indentation is applied in 10 equal load steps $\Delta a = 0.25$ up to the maximum value $a = 2.5$.

Deformed configurations obtained at two load levels are shown in Figure 10 for the mesh with $h = \frac{1}{9}$. As the indentation is increased, larger inter-element discontinuities appear in the upper-left portion of the domain, which can be attributed to the strongly imposed boundary conditions and the coarseness of the mesh. However, the global response is quite stable and in close agreement with the stable results presented in [27].

We also compare the final deformed configurations obtained on the three mesh resolutions in Figure 11. On the coarse mesh in Figure 11(a), discontinuities are reasonably significant throughout
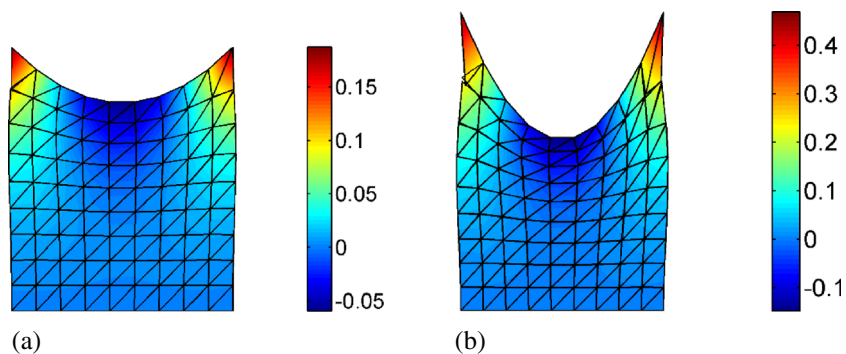
Figure 10. Vertical displacement u_2 superimposed on deformed configuration, mesh $h = 1/9$: (a) $a = 1.0$; (b) $a = 2.5$.
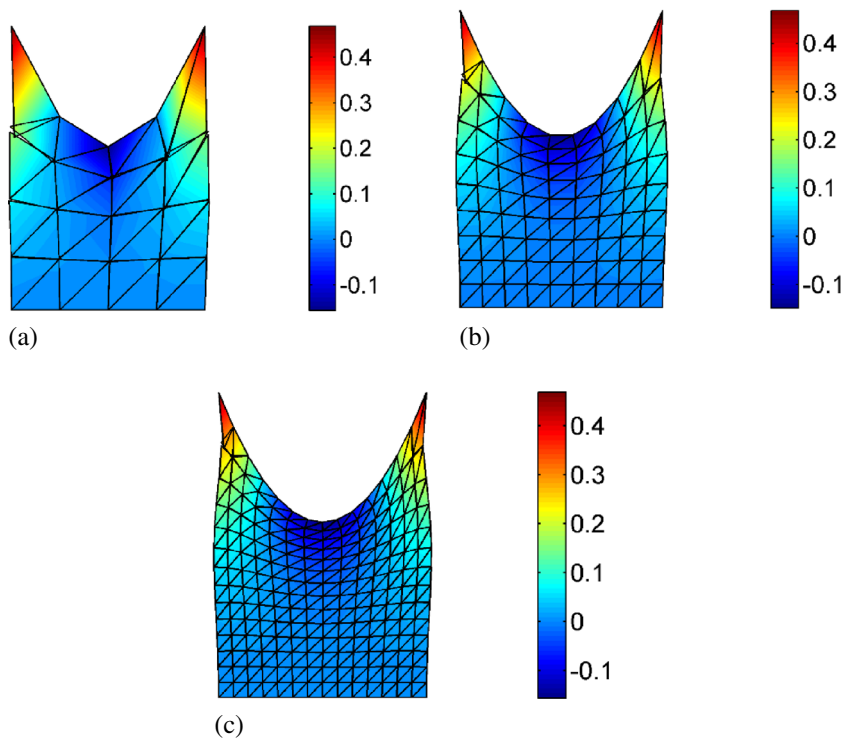
Figure 11. Vertical displacement u_2 superimposed on deformed configuration at load level $a = 2.5$: (a) $h = 1/4$; (b) $h = 1/9$; (c) $h = 1/14$.
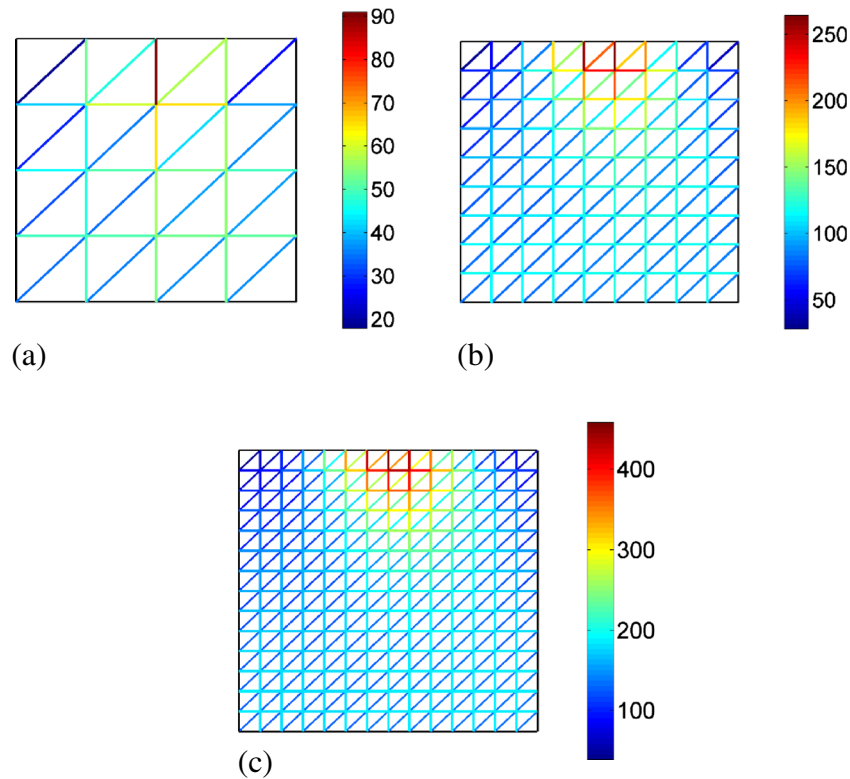
Figure 12. Wire-frame contour of stabilization tensor $\|\boldsymbol{\tau}_s\|$ along element edges: (a) $h = 1/4$; (b) $h = 1/9$; (c) $h = 1/14$.

the domain. A key attribute of DG methods as advocated in [27] is that coarse-mesh solutions can be obtained with improved accuracy in the gradient fields compared with continuous Galerkin (CG) approximations by relaxing inter-element continuity. Our results in Figure 11 agree qualitatively with that assessment, and the discontinuities steadily diminish as the mesh is refined. Additionally, across all meshes, the proposed formulation yields stable results free from spurious oscillations in the displacement jumps.

In order to examine the stabilization afforded by the fine-scale models, in Figure 12, we plot the norm of the penalty parameter $\|\boldsymbol{\tau}_s\| = \sqrt{\boldsymbol{\tau}_s : \boldsymbol{\tau}_s}$ computed according to (39) along each element interface at the final indentation level. The colors of the element edges in the mesh correspond to the magnitude of the parameter as denoted by the color bar. Clearly, significant spatial variability is present in the stabilization parameters. First, the magnitude of the parameters increases uniformly with mesh refinement while the distributions remain fairly consistent, indicating proper scaling with the element length scale [12, 27]. Thus, the remarks that follow apply equally to each of Figure 12(a)–12(c). Another common trend is that the values for diagonal edges are larger than those for edges aligned with the coordinate axes. Namely, the fine scales are attuned to the anisotropy induced in the discrete problem by isosceles triangular elements. More importantly, the values near the bowl of the parabola are about 5–10 times higher than the values observed throughout the rest of the domain. This results in more stabilization being applied in regions coinciding with the indefinite acoustic tensor, which agrees closely with the adaptive strategy considered in [27]. However, we emphasize that the trends presented here arise automatically from the fine-scale models (34) without any external calibration or monitoring.

Remark:
Similar spatial variation in the stabilization tensors was observed in the context of a VMS-stabilized method for finite mixed hyperelasticity [35], whereby the magnitude of the tensors was larger

in regions corresponding to larger stresses. Therein, the stabilization tensors are also derived in terms of fine-scale bubble functions and incorporate the constitutive material tensors. Thus, the strong link between the fine scales and the evolving coarse-scale deformations is shared with the present method.

Remark:
From the perspective of the cost of computation of the element-level quantities, the computation of the stability tensors $\boldsymbol{\tau}_s^{(\alpha)}$, $\boldsymbol{\tau}_s$, and $\boldsymbol{\delta}_s^{(\alpha)}$ add approximately one-third additional computational cost relative to the cost of evaluation of the residual vector and stiffness matrix associated with the interface terms as compared with using constant values for the parameters. In the opinion of the authors, this cost is offset by the benefits of having robust, nonlinearly evolving definitions of the parameters that require no calibration by the end user. This enables the confident application of the method to problems containing non-matching meshes, different element types, and heterogeneous material properties in the context of finite strains.

6.4. Finite deformation pure bending

In the fourth example problem, we investigate the performance of the proposed DG method under significant bending deformation. The domain of interest is a rectangular bar that is bent into an arc subtending an angle 2ψ, as illustrated in Figure 13. The solution for this plane strain problem is presented in Ogden [46] for an incompressible neo-Hookean material model, for which the deformation map $\boldsymbol{x} = \boldsymbol{\phi}(\boldsymbol{X})$ takes the following form:

$$\boldsymbol{x} = \begin{bmatrix} r\cos\theta \\ r\sin\theta \\ Z \end{bmatrix}, \qquad r(X) = \sqrt{\frac{2LX}{\psi} + R_o^2 - \frac{LH}{\psi}}, \qquad \theta(Y) = \frac{Y\psi}{L} \tag{62}$$

where R_o and R_i are the outer and inner radii, respectively, of the beam in the deformed configuration.

Notice that each longitudinal fiber of the beam originally parallel to the Y-axis is mapped into an arc of radius r, although this radius is not directly proportional to the original depth X of the fiber in the reference configuration. Additionally, the radius r and angle θ are separable functions of the reference coordinates X and Y, respectively. Therefore, the deformation gradient $\boldsymbol{F}$ can be expressed in the following simple form:
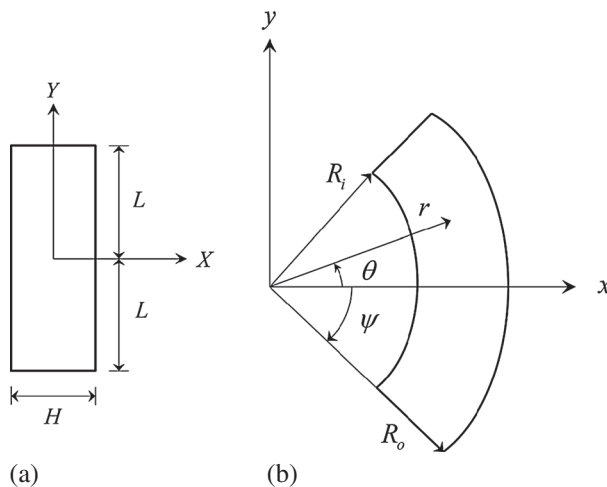

Figure 13. Pure bending of a rectangular beam: (a) undeformed configuration; (b) deformed configuration.

$$\boldsymbol{F} = \begin{bmatrix} (L/\psi r)\cos\theta & -(\psi r/L)\sin\theta & 0 \\ (L/\psi r)\sin\theta & (\psi r/L)\cos\theta & 0 \\ 0 & 0 & 1 \end{bmatrix} \tag{63}$$

It can be seen that the deformation represents pure bending because the off-diagonal components of the Green deformation tensor $\boldsymbol{C} = \boldsymbol{F}^T \boldsymbol{F}$ are identically zero and is also isochoric because $J = \det(\boldsymbol{F}) = 1$. To ensure globally incompressible response, the deformed and undeformed areas of the beam must be equal:

$$2HL = \psi\left(R_o^2 - R_i^2\right) \tag{64}$$

Furthermore, a second condition on the radii is obtained from the equilibrium equation [46] such that the tractions on the inner and outer surfaces vanish for an incompressible material:

$$(L/\psi)^2 = R_o R_i \tag{65}$$

For a given value of the bend angle ψ, the system of Equations (64)–(65) can be solved simultaneously to determine the relationships for R_i and R_o in order to express the deformed radius r solely in terms ψ (These rather lengthy expressions are not reported here). While this solution was originally derived for an ideal incompressible material, the deformation remains valid for a compressible material. Employing (63) within the constitutive law (56) results in the following expressions for the stress tensor and consistent body force for equilibrium:

$$\boldsymbol{P} = \left(\mu(L^2 - \psi^2 r^2)/\psi L r\right) \begin{bmatrix} \cos\theta & \sin\theta & 0 \\ \sin\theta & -\cos\theta & 0 \\ 0 & 0 & 0 \end{bmatrix} \tag{66}$$

$$\rho_o \boldsymbol{B} = \frac{\mu\kappa}{\psi^2 L^2 r^3} \begin{bmatrix} \cos\theta \\ \sin\theta \\ 0 \end{bmatrix}, \qquad \kappa = R_o^2 \psi^4 \left(2r^2 - R_o^2\right) + L^2\left(L^2 + \psi^2(H - 2X)^2\right) \tag{67}$$

Using this exact solution, we conduct a numerical convergence analysis on a sequence of uniformly refined meshes. Only the top half of the beam is modeled, and symmetry boundary conditions are applied to the mid-plane of the beam $Y = 0$. The traction field resulting from (66) is applied to all surfaces of the beam (including the mid-plane) along with the body force (67) throughout the domain. Although the surfaces $X = \pm W/2$ are traction free for an incompressible material due to the volumetric pressure field, this condition is lost for the compressible case. Uniform discretizations with quadrilateral and triangular elements are employed with fully discontinuous function spaces, where the coarsest quadrilateral mesh is 2×16 elements. Their performance will be benchmarked against the results from continuous finite element approximations on the same meshes. During the simulations, the bend angle ψ is increased up to a maximum value of π in increments $\Delta\psi = \pi/16$. We remark that because the applied forces from (66)-(67) are nonlinear functions of ψ, the consistent external nodal loads for the finite element mesh must be recomputed at each load step rather than proportionally incremented.

The bending stress $\sigma_{\theta\theta}$ plot for the 8×64 element mesh is illustrated on the deformed configuration of the beam for two load levels $\psi = \pi/2$ and $\psi = \pi$ in Figure 14. At the first load level, the discretized beam is almost bent into a quarter of a circular arc. Because the load level is controlled through force-type boundary conditions rather than prescribed displacement, the bend angle observed in the computed results will be less than the actual value. Furthermore, the displacement-based finite element methods typically produces approximations that are stiffer than the actual structure. Nonetheless, the deformed configuration in Figure 14(b) is approaching a half-circular arc and is fairly accurate for a coarse approximation.
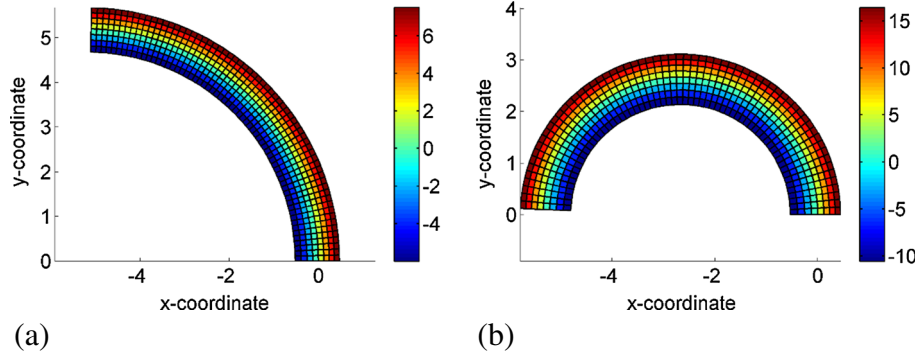
Figure 14. Stress $\sigma_{\theta\theta}$ on deformed configuration under pure bending of 8×64 quadrilateral mesh: (a) $\psi = \pi/2$; (b) $\psi = \pi$.
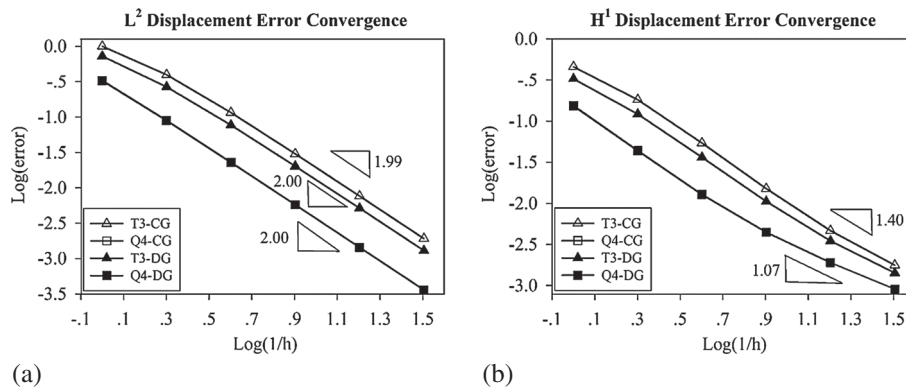

Figure 15. Convergence rate of displacement error norm for pure bending at bend angle $\psi = \frac{3\pi}{16}$: (a) L^2 norm; (b) H^1 seminorm.

To quantify the accuracy of the results, we compute the error in the displacement field $e = u - u^h$ obtained at each level of mesh refinement and record the value of the L^2 norm in Figure 15. The error norms are evaluated at the load level $\psi = 3\pi/16$. For nonlinear field theories, proving the theoretical convergence rate for the finite element method can be quite involved. However, the optimal rate of convergence for linear-interpolation elements from the linear field theory is a rate of 2.0 in the L^2 norm and 1.0 in the H^1 norm. We observe rates close to this optimal limit for the present analysis. Also, the triangular meshes contain a higher level of absolute error compared with the quadrilateral meshes, indicating that these elements are rather stiff, which is a common observation among discrete approximations with triangles [29]. However, the DG approximation does provide a slightly more accurate solution compared with CG for the same number of elements. This response indicates that the displacement jumps increase the flexibility of the discrete domain. The results for the DG and CG quadrilateral meshes are nearly identical.

As a final result, we determined the discrete angle ψ^h from the computed solution at each load level for comparison against the prescribed angle ψ and present the values in Figure 16. Because the deformation of the beam is driven by the applied tractions in terms of ψ, the actual deflection of the beam becomes a derived quantity for measuring the accuracy. We illustrate a consistent procedure for determining the angle ψ^h in Figure 16(a). First, a line segment is drawn connecting the endpoints A and B of the beam. Next, a perpendicular bisector CD is constructed, where the point D is located at the intersection with the horizontal axis. Finally, the angle ψ^h between line segments AD and BD is calculated using the law of cosines. This angle is determined for four of the quadrilateral DG meshes and plotted in Figure 16(b); the angle is measured in radians, and n indicates the number of elements through the thickness of the beam. Clearly, the exact curve is $\psi^h = \psi$, a line with a slope
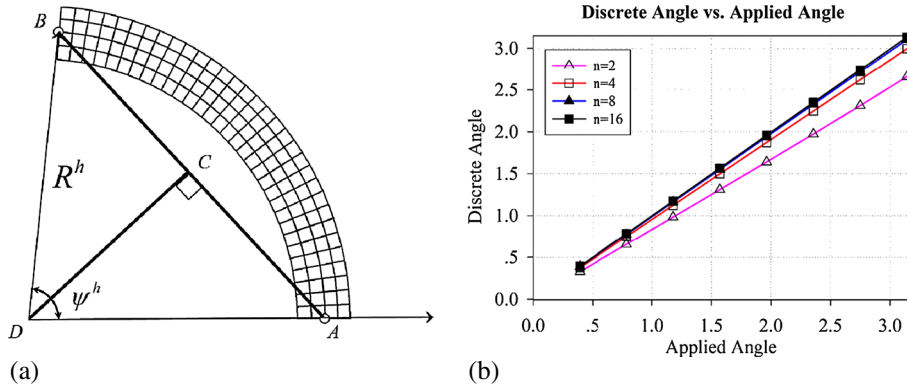
Figure 16. Discrete angle ψ^h for pure bending: (a) determination from computed results; (b) discrete angle ψ^h versus prescribed angle ψ for DG method.
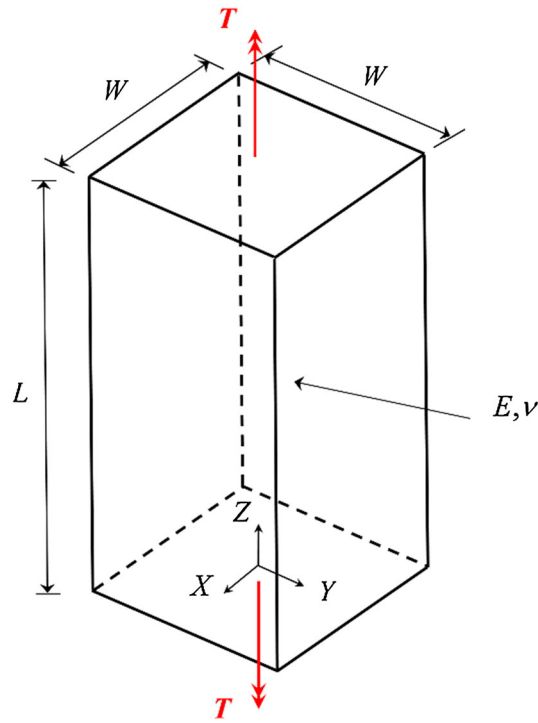

Figure 17. Rectangular bar under longitudinal torsion.

of one. We observe that as the mesh is refined, the values from the quadrilateral DG meshes converge to the correct result. Similar trends were obtained for the CG method and the triangular meshes.

6.5. Torsion at finite strains

For the final numerical problem, we consider a rectangular bar subjected to torsion, as shown in Figure 17. A deformation map that induces longitudinal twist to the bar can be expressed as follows:

$$\boldsymbol{x} = \boldsymbol{R}(\theta) \cdot \boldsymbol{X}, \qquad \boldsymbol{R}(\theta) = \begin{bmatrix} \cos\theta & -\sin\theta & 0 \\ \sin\theta & \cos\theta & 0 \\ 0 & 0 & 1 \end{bmatrix}, \qquad \theta(Z) = \frac{2\pi Z \psi}{L} \tag{68}$$

where L is the length of the bar and the parameter ψ represents the number of complete revolutions of the top face of the bar with respect to the bottom face. This deformation mode is described in [46], where the expressions have been converted from cylindrical to Cartesian components by using the trigonometric identity concerning the summation of angles. Similar to the problems in Sections 6.2 and 6.4, equation (68) is taken as the exact solution, and the surface tractions and body force required for equilibrium are derived and applied within the computational model. The resulting expressions for $\boldsymbol{F}$, $\boldsymbol{P}$, and $\boldsymbol{B}$ are given by

$$\boldsymbol{F} = \begin{bmatrix} \cos\theta & -\sin\theta & 2\pi(\psi/L)(-Y\cos\theta - X\sin\theta) \\ \sin\theta & \cos\theta & 2\pi(\psi/L)(X\cos\theta - Y\sin\theta) \\ 0 & 0 & 1 \end{bmatrix} \tag{69}$$

$$\boldsymbol{P} = 2\pi\mu(\psi/L) \begin{bmatrix} 0 & 0 & -Y\cos\theta - X\sin\theta \\ 0 & 0 & X\cos\theta - Y\sin\theta \\ -Y & X & 0 \end{bmatrix} \tag{70}$$

$$\rho_o \boldsymbol{B} = \mu\left[2\pi(\psi/L)\right]^2 \begin{bmatrix} X\cos\theta - Y\sin\theta \\ Y\cos\theta + X\sin\theta \\ 0 \end{bmatrix} \tag{71}$$

where $\mu = E/2(1+\nu)$ again is the shear modulus. Note that the deformation induces pure shear and is thus isochoric, namely $J = 1$. Therefore, this problem will be used to test the performance of the DG method for large shearing and rotational effects.

In the benchmark study herein, the dimensions of the bar are taken as $L = 4$ and $W = 2$ along with the material properties $E = 100$ and $\nu = 0.25$. Uniform meshes of linear tetrahedral elements and trilinear hexahedral elements are employed with fully discontinuous approximations between each element. The coarsest mesh consists of $2 \times 2 \times 8$ hexahedral elements, and the tetrahedral meshes are formed by subdividing each hexahedral element into six tetrahedra, similar to [35]. Again, continuous finite element approximations will serve as a reference. The bottom face of the bar is held fixed in the Z-direction and prevented from rigid-body rotation by restraining the middle node along each edge. Surface tractions according to $\boldsymbol{T} = \boldsymbol{P} \cdot \boldsymbol{N}$ from (70) are applied to all faces of the bar; in particular, the vertical faces have nonzero tractions because the cross section is not circular.

For a series of uniformly refined meshes, simulations were conducted in which the bar was twisted to a maximum revolution of $\psi = 2$ at equal intervals of $\Delta\psi = 0.125$. Representative deformed configurations of the bar are shown in Figure 18 for two load levels on the crudest $2\times2\times8$ element mesh and a refined mesh. The superimposed contour plot represents the value of the torsional Cauchy stress $\sigma_{z\theta}$ computed at the center of each element from the DG approximations. For planes of elements parallel to the X–Y plane, we observe a constant value of the torsional stress for elements that are equidistant from the longitudinal axis, which agrees with the intuition from the classical mechanics of materials. Namely, as the mesh is refined, the computed solution more closely captures the linearly varying torsional stress in the radial direction. This is evidenced by the similar magnitude but increased resolution provided between Figure 18(a) and 18(c) at load level $\psi = 0.5$ and similarly for Figure 18(b) and 18(d). Moreover, the level of stress remains constant along the length of the bar in the computed results and does not show any decay or spurious features. Note that these stresses are computed in the rotated coordinate system obtained from the deformed configuration of the mesh. The uniformity of the results obtained both in the longitudinal and in the transverse directions is a testimony to the accuracy of the results. In particular, significant deformations are present at the load level $\psi = 1.0$ as evidenced in Figure 18(b) and 18(d).

Because this problem has an exact solution, we compute the displacement discretization error obtained on each mesh and plot the value of the L^2 norm and H^1 seminorm in Figure 19(a) and (b), respectively, at the loading stage $\psi = 0.125$. For this problem, the DG approximation outperforms
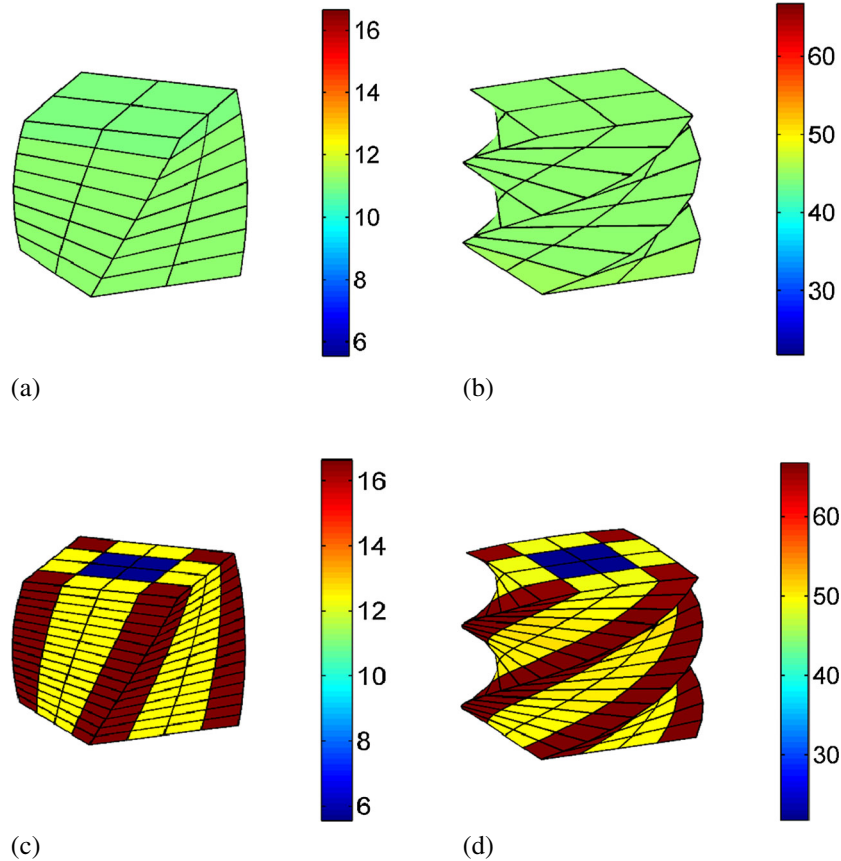
Figure 18. Stress $\sigma_{z\theta}$ on deformed configuration at two load levels: (a) $h = 2$; $\psi = 0.125$; (b) $h = 2$; $\psi = 0.5$; (c) $h = 4$; $\psi = 0.125$; (d) $h = 4$; $\psi = 0.5$.

the CG approximation for tetrahedral elements in both error measures. Also, the optimal convergence rate of 1.0 in the H^1 seminorm is obtained by each of the element types. These smooth trends are a strong indicator of the stability of the results. The convergence rates in the L^2 norm are fairly optimal for the tetrahedral elements. The hexahedral meshes also exhibit slightly suboptimal performance in the field norm upon mesh refinement; however, the convergent results of the gradients indicate that these elements are stable nonetheless.

By inspecting the deformation map (68) as well as considering the response of the bar in Figure 18, we observe that the response is quasi-periodic. Namely, the response of a bar with length nL could be obtained by simulating one bar of length L and appending n copies of the response end to end, with appropriate rigid rotations applied to match the bases from each section. Furthermore, the traction field on cross sections parallel to the X–Y plane with normal $N = E_3$ takes the following simple form according to (70):

$$
\begin{aligned}
P \cdot E_3 &= 2\pi\mu(\psi/L)\left[-Y\cos\theta - X\sin\theta, \ X\cos\theta - Y\sin\theta, \ 0\right]^T \\
&= 2\pi\mu(\psi/L)R^\perp(\theta) \cdot (X - ZE_3) \equiv 2\pi\mu(\psi/L)R^\perp(\theta) \cdot X_{12}
\end{aligned}
\tag{72}
$$

where $R^\perp$ is the tensor that produces rotations, which are orthogonal to R, such that $(R \cdot X_{12}) \cdot (R^\perp \cdot X_{12}) = 0$. This traction vector clearly lies in the plane of the cross section, is perpendicular to the twisted radial vector $R \cdot X_{12}$, and has a magnitude equal to $2\pi\mu(\psi/L)$ when normalized by the radial distance. An example of these vectors is provided in Figure 20(a).

Now suppose that two different bars undergo torsion such that $\mu^{(1)}\left(\psi^{(1)}/L^{(1)}\right) = \mu^{(2)}\left(\psi^{(2)}/L^{(2)}\right) = C$. According to (72), the cross sections of each bar would experience the same traction field. This thought experiment suggests a possible sophistication of the previous problem to a bar consisting of two materials, which is illustrated in Figure 20(b). In light of the previous discussion, we obtain the solution for the deformed shape of the upper portion of the bar simply by rotating and translating the general expressions (68)-(71):

$$x' = \boldsymbol{Q}_\theta \cdot \boldsymbol{x}(X'), \qquad \boldsymbol{T}' = \boldsymbol{Q}_\theta \cdot \boldsymbol{P}(X') \cdot \boldsymbol{N}, \qquad \boldsymbol{B}' = \boldsymbol{Q}_\theta \cdot \boldsymbol{B}(X') \tag{73}$$

where the translated coordinate is $X' = X - L^{(1)}\boldsymbol{E}_3$ and the rotation tensor $\boldsymbol{Q}_\theta = \boldsymbol{R}(2\pi\psi^{(1)})$ reorients the bases of the bars to match at the interface. The expressions in (73) are evaluated in terms of the properties $\mu^{(2)}, \psi^{(2)}, L^{(2)}$ for the second portion of the bar. These results align with the classical strength of materials theory: when a composite rod is subjected to torsion, the twist experienced by each component is inversely proportional to its shear modulus while the torqueing moment in each component remains constant.
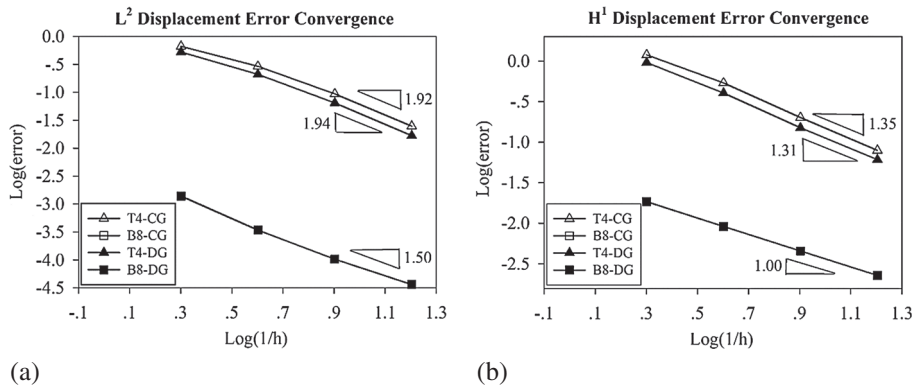

Figure 19. Convergence rates of displacement error for longitudinal torsion at load level $\psi = 0.125$: (a) L^2 norm; (b) H^1 seminorm.
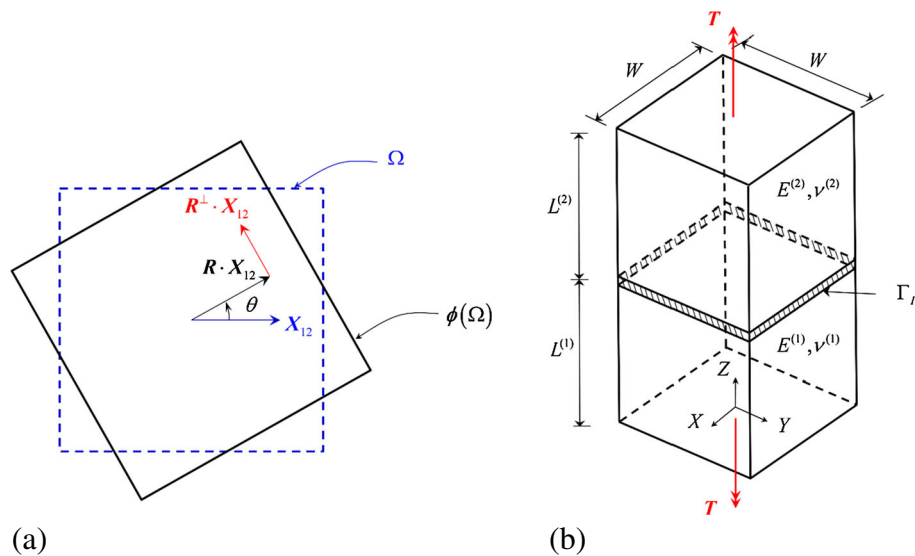

Figure 20. Enhanced torsion problem: (a) traction vector on twisted cross section; (b) bi-material rectangular bar.
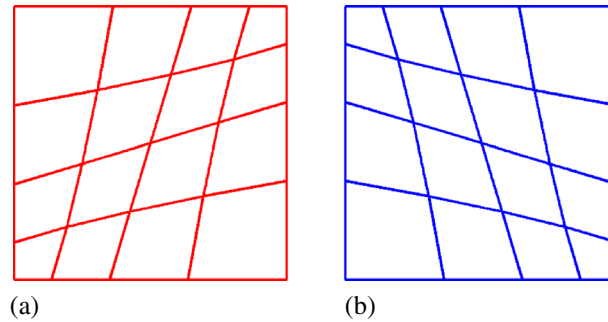
Figure 21. Plan view of nonconforming coarse mesh: (a) bottom region; (b) top region.
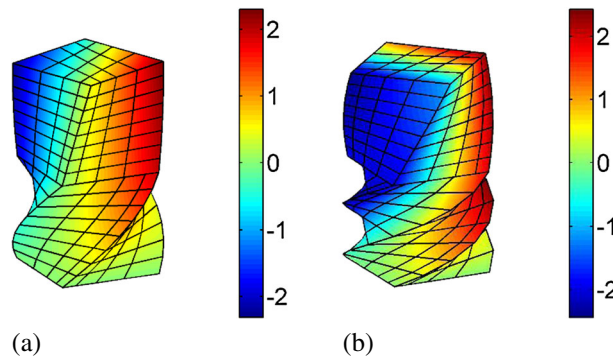

Figure 22. Displacement u_x contour plot on the deformed shape for the bi-material torsion problem: (a) load level $\psi^{(1)} = 0.25$; (a) load level $\psi^{(1)} = 0.5$.

For the numerical tests that follow, we adopt the geometric and material properties $L^{(1)} = L^{(2)} = 2$, $W = 2$, $E^{(1)} = 100$, $E^{(2)} = 400$, and $\nu^{(1)} = \nu^{(2)} = 0.25$. Also, to make this test more stringent, the portions of the bar are discretized in a biased fashion to create a nonconforming mesh in the zone of the material interface. Plan views of the coarse meshes for the top and bottom portions of the bar are shown in Figure 21; subsequent meshes are obtained by bisecting this discretization. Within the remainder of the bar, continuous finite element approximations are employed. This problem is a good test case for a unified CG–DG method under large rotational effects wherein potential weak discontinuities from material mismatch can evolve into strong discontinuities such as debonding. Therefore, it serves as a test bed for mathematically nonsmooth problems under evolving finite rotations.

The response of the bar is simulated on the coarse mesh by increasing the twist angle $\psi^{(1)}$ in increments $\Delta\psi^{(1)} = 0.125$ and computing applied tractions and body forces on both regions, with $\psi^{(2)} = \psi^{(1)}/4$. The deformed configuration of the domain is shown in Figure 22 for two representative load levels. We highlight that the top half of the bar indeed twists less than the lower portion. However, both the displacement field and the tractions are continuous at the interface. Spurious gaps have not opened up between the nonconforming meshes, and the discrete solution is quite smooth. Thus, the stabilized interface formulation provides very accurate results for this challenging problem.

To further investigate the properties at the nonconforming interface, we compute some quantities of interest such as the magnitude of the discrete interface gap $[\![\phi]\!]$ and the interface numerical flux vector, which are shown in Figure 23. The contour of the interface gap $[\![\phi]\!]$ is not symmetric because of the differing bias in the top and bottom meshes along with the fact that the loading and deformed configuration in Figure 22 do not display symmetry. However, the jump is three orders of magnitude smaller than the displacement field, indicating that the discontinuities are well controlled. Also, the traction field at the interface appears quite smooth in Figure 23(b), where the edge lines have been
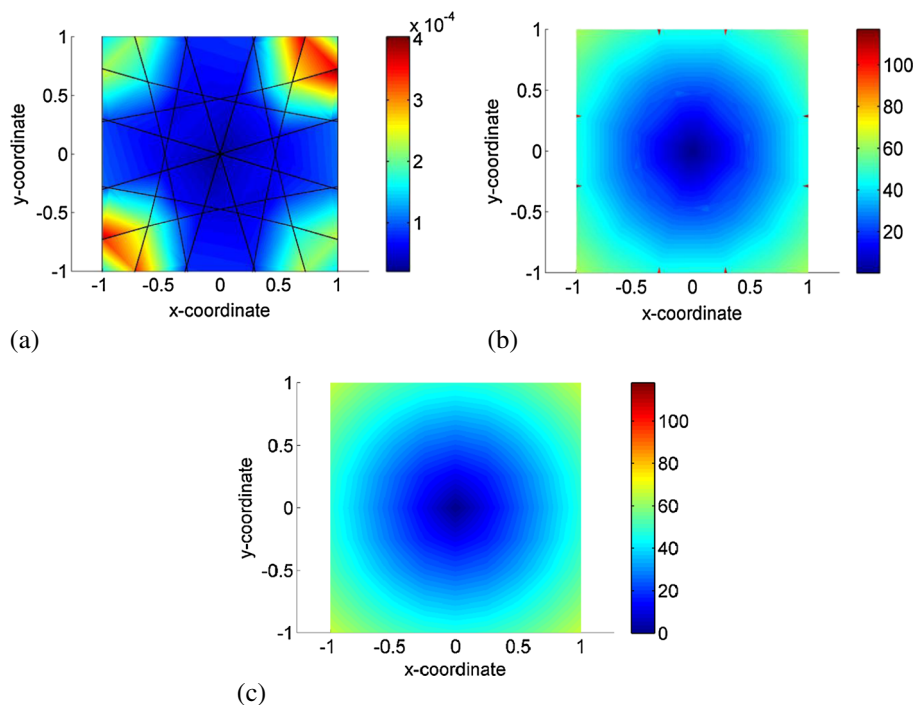
Figure 23. Contour plots at material interface for twist $\psi^{(1)} = 0.375$: (a) magnitude of discrete interface gap $[\![\boldsymbol{\phi}]\!]$; (b) magnitude of numerical flux vector; (c) exact interface stress $\sigma_{z\theta}$.

removed for clarity. Note that the total numerical flux $\boldsymbol{\lambda} = \{\boldsymbol{P} \cdot \boldsymbol{N}\} - \boldsymbol{\tau}_s \cdot [\![\boldsymbol{\phi}]\!]$ as given by (38) containing both the average traction and the penalty term is plotted in the figure, which is traditionally the defining measure of interface stress [4, 19]. Slight over-predictions of the numerical flux, indicated by the red color contour, are present in the extremely small triangular interface segments formed from slightly mismatched nodes in the upper and lower portions of the bar. These artifacts are generated by the over-prediction of the penalty tensor $\boldsymbol{\tau}_s$ in these segments, which is an issue similar to that encountered in embedded mesh techniques in the presence of vanishingly small cut elements [4]. Nonetheless, the accuracy of the computed stresses compared with the exact stress in Figure 23(c) is a testament to the quality of the stability tensors derived from the fine-scale models (35) in the presence of significant geometric and material mismatch.

7. CONCLUSIONS

In this work, we derive a DG interface formulation for finite strain kinematics by extending the developments for linear elasticity contained in the general framework of [19]. A Lagrange multiplier treatment of the interface continuity constraints serves as the starting point for the derivation, and this mixed field problem is stabilized by invoking concepts from the VMS method. Herein, a distinguishing feature is that the localized fine-scale problems at the interface are consistently linearized in order to develop analytical models for the fine-scale displacement field. By embedding these fine-scale models into the coarse-scale problem, enhanced stability is obtained that subsequently enables the Lagrange multipliers to be condensed from the formulation, leading to a primal weak form analogous to the DG method. Through the fine-scale stabilization process, closed-form expressions are obtained for the numerical flux and penalty parameter that vary from element to element based on the material properties and local mesh topology at the interface. Unique to the present nonlinear context, these fine-scale models evolve with the local material and geometric nonlinearity of the bulk domain in the vicinity of the interface. By accounting for the complete spectrum of the constitutive material model, element geometry and length scale, and nonlinear effects, the robust definitions for

the numerical flux and penalty parameter herein adaptively compensate for instabilities that may arise under increasing deformations.

To facilitate the implementation of the method, we represent the fine-scale fields using simple polynomial bubble functions, similar to those previously investigated in the context of small strains [19]. While the method was originally developed for imposing continuity weakly over nonconforming meshes within a domain, a natural extension of the ideas yields a formulation accommodating fully discontinuous approximations over the discretized domain. Both versions of the method, enforcing continuity across nonconforming interfaces or across inter-element boundaries, are investigated through a series of two-dimensional and three-dimensional test problems that cover a range of deformation modes. Particular emphasis is placed on problems incorporating significant bending and torsional effects to verify that the fine-scale models remain objective and provide stability under large strains. In all cases, accurate results were obtained from the method by using the form of the stability parameters derived herein without additional calibration. Strong performance is exhibited by both triangular and quadrilateral elements along with their higher-dimensional counterparts for problems with material mismatch and significant mesh nonconformity. Error convergence analyses were conducted for problems with analytical solutions, and the convergence of the discretization error confirmed the stability of the proposed interface method. The next logical steps for extending this formulation, which we plan to pursue, are the treatment of history-dependent material response as well as the treatment of evolving strong discontinuities such as delamination.

APPENDIX A

The derivations in Section 3 have been carried out in the reference configuration in terms of the first Piola–Kirchhoff stress P and the acoustic tensor A so that the resulting interface formulation (48) can be expressed in a form closely resembling the small strain counterpart [19]. An entirely equivalent representation can be written using the second Piola–Kirchhoff stress S and the material tangent tensor C by recourse to transformations from continuum mechanics [41, 44]:

$$P_{iJ} = F_{iI} S_{IJ} \tag{A.1}$$

$$A_{iIjJ} = g_{ij} S_{IJ} + F_{iK} F_{jL} C_{KILJ} \tag{A.2}$$

where g is the spatial metric tensor and, throughout the following discussion, lower-case and upper-case subscripts refer to components expressed in current and reference coordinate systems, respectively. Expressions for S and C arise in the usual manner by differentiating the strain energy density function W with respect to the Green–Lagrange strain tensor E. By carefully differentiating (A.2), we obtain the following relation for the sixth-order material tangent tensor D that was defined in [41]:

$$\Xi_{iIjJkK} = g_{ij} F_{kL} C_{IJLK} + g_{ik} F_{jL} C_{KILJ} + g_{jk} F_{iL} C_{JKLI} + F_{iL} F_{jM} F_{kN} D_{LIMJNK} \tag{A.3}$$

Notice that Ξ possesses major symmetry for each pair of dual-basis components because of the symmetries of C and D.

To obtain the spatial counterpart of the weak form (48) and the linearized form (54), we require the following transformation relations for the Cauchy stress tensor σ, spatial tangent tensor c, and spatial sixth-order tensor d:

$$
\begin{aligned}
J\sigma_{ij} &= F_{iI} S_{IJ} F_{jJ}, \\
Jc_{ijkl} &= F_{iI} F_{jJ} C_{IJKL} F_{kK} F_{lL}, \\
Jd_{ijklmn} &= F_{iI} F_{jJ} F_{kK} D_{IJNKLMN} F_{lL} F_{mM} F_{nN}
\end{aligned}
\tag{A.4}
$$

where $J = \det(F)$. Furthermore, we will use the following transformation of area and surface infinitesimal elements as well as the unit normal vector N:

$$\mathrm{d}v = J\mathrm{d}V, \quad \boldsymbol{n}\mathrm{d}a = J\boldsymbol{F}^{-T}\boldsymbol{N}\mathrm{d}A, \quad \mathrm{d}a/\mathrm{d}A \equiv \vartheta_A^{-1} = J\left\|\boldsymbol{F}^{-T}\boldsymbol{N}\right\| \tag{A.5}$$

where $\boldsymbol{n}$ is the unit outward normal to the deformed domain $\boldsymbol{\phi}(\Omega)$. The last expression (A.5) has a very important implication: in the discrete setting, the mapped unit vectors $\boldsymbol{n}^{(\alpha)}$ in the spatial configuration on either side of the interface Γ_I will not be identical in general. This observation is due to the dependence of the unit normal on the deformation gradient $\boldsymbol{F}^{(\alpha)}$, which may take distinct values across the interface when continuity and equilibrium are enforced only in a weak sense through (4) and (5). Therefore, numerical integration in the deformed configuration must take this consideration into account. Additionally, the differential area element $\mathrm{d}a$ for each side of the interface may also be different because of the discontinuity of $\boldsymbol{F}$.

We omit the details of substituting the transformations (A.1)-(A.5) within the weak form (48) and provide the final results:

$$
\begin{aligned}
R\left(\boldsymbol{\eta}^{(\alpha)}, \boldsymbol{\phi}^{(\alpha)}\right) = &\sum_{\alpha=1}^{2} \int_{\boldsymbol{\phi}^{(\alpha)}(\Omega^{(\alpha)})} \left[\nabla^{\mathrm{s}}\boldsymbol{\eta}^{(\alpha)} : \boldsymbol{\sigma}^{(\alpha)} - \boldsymbol{\eta}^{(\alpha)} \cdot \rho^{(\alpha)}\boldsymbol{B}^{(\alpha)}\right]\mathrm{d}v \\
&- \sum_{\alpha=1}^{2} \int_{\boldsymbol{\phi}^{(\alpha)}(\Gamma_I)} (-1)^{\alpha-1}[\![\boldsymbol{\eta}]\!] \cdot \left(\boldsymbol{\delta}_s^{(\alpha)} \cdot \boldsymbol{\sigma}^{(\alpha)} \cdot \boldsymbol{n}^{(\alpha)}\right)\mathrm{d}a \\
&- \sum_{\alpha=1}^{2} \int_{\boldsymbol{\phi}^{(\alpha)}(\Gamma_I)} (-1)^{\alpha-1}\left[\boldsymbol{\delta}_s^{(\alpha)} \cdot \left(\nabla^s\boldsymbol{\eta}^{(\alpha)} : \boldsymbol{c}^{(\alpha)}\right) \cdot \boldsymbol{n}^{(\alpha)}\right] \cdot [\![\boldsymbol{\phi}]\!]\mathrm{d}a \\
&+ \sum_{\alpha=1}^{2} \int_{\boldsymbol{\phi}^{(\alpha)}(\Gamma_I)} (-1)^{\alpha-1}\boldsymbol{\eta}^{(\alpha)} \cdot \boldsymbol{\tau}_s \cdot [\![\boldsymbol{\phi}]\!]\,\vartheta_A\mathrm{d}a = 0
\end{aligned}
\tag{A.6}
$$

where $\boldsymbol{\eta}^{(\alpha)} = \boldsymbol{\eta}_o^{(\alpha)} \circ \left(\boldsymbol{\phi}^{(\alpha)}\right)^{-1}$ is the spatial displacement variation, $\nabla(\cdot) = \partial(\cdot)/\partial x$ is the spatial gradient, $\nabla^{\mathrm{s}}(\cdot) = \frac{1}{2}\left[\nabla(\cdot) + (\nabla(\cdot))^T\right]$, and $\rho = J^{-1}\rho_o$ is the spatial density. The values of the stabilization tensors $\boldsymbol{\tau}_s$ and $\boldsymbol{\delta}_s^{(\alpha)}$ are unaffected by the transformation. However, if desired, the stability tensors $\boldsymbol{\tau}_s^{(\alpha)}$ may be evaluated in the spatial configuration by pushing forward (33) as follows:

$$
\tilde{\boldsymbol{\tau}}_s^{(\alpha)} = \left[\int_{\boldsymbol{\phi}^{(\alpha)}\left(\omega_s^{(\alpha)}\right)} \nabla\boldsymbol{b}_s^{(\alpha)} \cdot \left(\boldsymbol{\sigma}^{(\alpha)} \cdot \nabla\boldsymbol{b}_s^{(\alpha)}\right) + \nabla\boldsymbol{b}_s^{(\alpha)} : \boldsymbol{c}^{(\alpha)} : \nabla\boldsymbol{b}_s^{(\alpha)}\mathrm{d}v\right]^{-1} \tag{A.7}
$$

Finally, the spatial counterpart of the linearized weak form (54) is presented in (A.8):

$$
\begin{aligned}
K\left(\boldsymbol{\eta}^{(\alpha)}, \Delta\boldsymbol{u}^{(\alpha)}; \boldsymbol{\phi}^{(\alpha)}\right) = &\sum_{\alpha=1}^{2} \int_{\boldsymbol{\phi}^{(\alpha)}(\Omega^{(\alpha)})} \left(\nabla\boldsymbol{\eta}^{(\alpha)} \cdot \left(\boldsymbol{\sigma}^{(\alpha)} \cdot \nabla\boldsymbol{\eta}^{(\alpha)}\right) + \nabla^{\mathrm{s}}\boldsymbol{\eta}^{(\alpha)} : \boldsymbol{c}^{(\alpha)} : \nabla^{\mathrm{s}}\boldsymbol{\eta}^{(\alpha)}\right)\mathrm{d}v \\
&+ \sum_{\alpha=1}^{2} \int_{\boldsymbol{\phi}^{(\alpha)}(\Gamma_I)} (-1)^{\alpha-1}\boldsymbol{\eta}^{(\alpha)} \cdot \boldsymbol{\tau}_s \cdot [\![\Delta\boldsymbol{u}]\!]\,\vartheta_A\mathrm{d}a \\
&- \sum_{\alpha=1}^{2} \int_{\boldsymbol{\phi}^{(\alpha)}(\Gamma_I)} (-1)^{\alpha-1}[\![\boldsymbol{\eta}]\!] \cdot \left[\boldsymbol{\delta}_s^{(\alpha)} \cdot \left(\boldsymbol{c}^{(\alpha)} : \nabla^{\mathrm{s}}\left(\Delta\boldsymbol{u}^{(\alpha)}\right)\right) \cdot \boldsymbol{n}^{(\alpha)}\right]\mathrm{d}a \\
&- \sum_{\alpha=1}^{2} \int_{\boldsymbol{\phi}^{(\alpha)}(\Gamma_I)} (-1)^{\alpha-1}\left[\boldsymbol{\delta}_s^{(\alpha)} \cdot \left(\nabla^{\mathrm{s}}\boldsymbol{\eta}^{(\alpha)} : \boldsymbol{c}^{(\alpha)}\right) \cdot \boldsymbol{n}^{(\alpha)}\right] \cdot [\![\Delta\boldsymbol{u}]\!]\mathrm{d}a \\
&- \sum_{\alpha=1}^{2} \int_{\boldsymbol{\phi}^{(\alpha)}(\Gamma_I)} (-1)^{\alpha-1}\left[\boldsymbol{\delta}_s^{(\alpha)} \cdot K_{uu}\left(\boldsymbol{\eta}^{(\alpha)}, \Delta\boldsymbol{u}^{(\alpha)}; \boldsymbol{\phi}^{(\alpha)}\right) \cdot \boldsymbol{n}^{(\alpha)}\right] \cdot [\![\boldsymbol{\phi}]\!]\mathrm{d}a
\end{aligned}
\tag{A.8}
$$

and the additional stiffness term is defined as follows, where the superscripts (α) have been suppressed:

$$
\begin{aligned}
K_{uu}(\boldsymbol{\eta}, \Delta\boldsymbol{u}; \boldsymbol{\phi}) = \nabla\boldsymbol{\eta} \cdot [\boldsymbol{c} : \nabla^s(\Delta\boldsymbol{u})] + \nabla(\Delta\boldsymbol{u}) \cdot [\boldsymbol{c} : \nabla^s\boldsymbol{\eta}] \\
+ [(\boldsymbol{d} : \nabla^s(\Delta\boldsymbol{u})) : \nabla^s\boldsymbol{\eta}] + \boldsymbol{c} : \left[(\nabla(\Delta\boldsymbol{u}))^T \cdot \nabla\boldsymbol{\eta}\right]
\end{aligned}
\tag{A.9}
$$

APPENDIX B

Here, we provide the expressions for the material tensors corresponding to the strain energy density function (56); a similar material model was considered in [10].

First Piola–Kirchhoff stress tensor $\boldsymbol{P}$:

$$
P_{iI} = \mu\left(F_{Ii}^{-1} + F_{iI}\right) + \lambda J(J-1)F_{Ii}^{-1}
\tag{B.1}
$$

Acoustic tensor **A**:

$$
A_{iIjJ} = \mu\left(F_{Ij}^{-1}F_{Ji}^{-1} + g_{ij}G_{IJ}^{-1}\right) + \lambda\left[J(2J-1)F_{Ii}^{-1}F_{Jj}^{-1} - J(J-1)F_{Ij}^{-1}F_{Ji}^{-1}\right]
\tag{B.2}
$$

Sixth-order material tensor $\boldsymbol{\Xi}$:

$$
\begin{aligned}
\Xi_{iIjJkK} = \left[\lambda J(J-1) - \mu\right]\left(F_{Jk}^{-1}F_{Ki}^{-1}F_{Ij}^{-1} + F_{Ji}^{-1}F_{Ik}^{-1}F_{Kj}^{-1}\right) + \lambda\left[J(4J-1)F_{Ii}^{-1}F_{Jj}^{-1}F_{Kk}^{-1}\right] \\
- \lambda J(2J-1)\left[F_{Ik}^{-1}F_{Ki}^{-1}F_{Jj}^{-1} + F_{Ii}^{-1}F_{Jk}^{-1}F_{Kj}^{-1} + F_{Kk}^{-1}F_{Ji}^{-1}F_{Ij}^{-1}\right]
\end{aligned}
\tag{B.3}
$$

where $\boldsymbol{G}^{-1}$ is the inverse of the material metric tensor. The spatial constitutive tensors take a much simpler form.

Cauchy stress tensor $\boldsymbol{\sigma}$:

$$
J\sigma_{ij} = \mu\left(g_{ij}^{-1} + F_{iI}F_{jI}\right) + \lambda J(J-1)g_{ij}^{-1}
\tag{B.4}
$$

Spatial tangent tensor c:

$$
Jc_{ijkl} = \mu\left(g_{ik}^{-1}g_{jl}^{-1} + g_{il}^{-1}g_{jk}^{-1}\right) + \lambda\left[J(2J-1)g_{ij}^{-1}g_{kl}^{-1} - J(J-1)\left(g_{ik}^{-1}g_{jl}^{-1} + g_{il}^{-1}g_{jk}^{-1}\right)\right]
\tag{B.5}
$$

Table B.1. Components of spatial sixth-order volumetric tensor.

Component	Value	Condition
$[\boldsymbol{d}_1]_{iijjkk}$	1	None
$[\boldsymbol{d}_2]_{iiiiii}$	-6	None
$[\boldsymbol{d}_2]_{iiiijj}$	-2	$i \neq j$
$[\boldsymbol{d}_2]_{iijkjk}$	-1	$j \neq k$
$[\boldsymbol{d}_3]_{iiiiii}$	8	None
$[\boldsymbol{d}_3]_{iiijij}$	2	$i \neq j$
$[\boldsymbol{d}_3]_{iijkki}$	1	$i \neq j \neq k$

Sixth-order material tensor $\boldsymbol{d}$:

$$Jd_{ijklmn} = [\lambda J(J-1) - \mu](\boldsymbol{d}_3)_{ijklmn} + \lambda\left[J(4J-1)(\boldsymbol{d}_1)_{ijklmn}\right]$$
$$+ \lambda J(2J-1)(\boldsymbol{d}_2)_{ijklmn} \tag{B.6}$$

where the tensors $\boldsymbol{d}_1, \boldsymbol{d}_2$, and $\boldsymbol{d}_3$ are defined in [35], and the values of their components in a Cartesian coordinate frame are listed in Table B.1.

REFERENCES

1. Hansbo P, Larson MG. Discontinuous Galerkin methods for incompressible and nearly incompressible elasticity by Nitsche's method. *Computer Methods in Applied Mechanics and Engineering* 2002; **191**(17):1895–1908.
2. Ten Eyck A, Lew A. Discontinuous Galerkin methods for non-linear elasticity. *International Journal for Numerical Methods in Engineering* 2006; **67**(9):1204–1243.
3. Truster TJ, Masud A. A discontinuous/continuous Galerkin method for modeling of interphase damage in fibrous composite systems. *Computational Mechanics* 2013; **52**:499–514.
4. Annavarapu C, Hautefeuille M, Dolbow JE. A robust Nitsche's formulation for interface problems. *Computer Methods in Applied Mechanics and Engineering* 2012; **225**:44–54.
5. Sanders JD, Laursen TA, Puso MA. A Nitsche embedded mesh method. *Computational Mechanics* 2012; **49**(2): 243–257.
6. Johnson C, Nävert U, Pitkäranta J. Finite element methods for linear hyperbolic problems. *Computer Methods in Applied Mechanics and Engineering* 1984; **45**(1):285–312.
7. Arnold DN. An interior penalty finite element method with discontinuous elements. *SIAM Journal on Numerical Analysis* 1982; **19**(4):742–760.
8. Nitsche J. Über ein Variationsprinzip zur Lösung von Dirichlet-Problemen bei Verwendung von Teilräumen, die keine Randbedingungen untervorfen sind. *Abhandlungen in der Mathematik an der Universität Hamburg* 1971; **36**:9–15.
9. Masud A, Truster TJ, Bergman LA. A unified formulation for interface coupling and frictional contact modeling with embedded error estimation. *International Journal for Numerical Methods in Engineering* 2012; **92**(2):141–177.
10. Mergheim J, Steinmann P. A geometrically nonlinear FE approach for the simulation of strong and weak discontinuities. *Computer Methods in Applied Mechanics and Engineering* 2006; **195**(37):5037–5052.
11. Bazilevs Y, Michler C, Calo VM, Hughes TJR. Weak Dirichlet boundary conditions for wall-bounded turbulent flows. *Computer Methods in Applied Mechanics and Engineering* 2007; **196**(49):4853–4862.
12. Arnold DN, Brezzi F, Cockburn B, Marini LD. Unified analysis of discontinuous Galerkin methods for elliptic problems. *SIAM Journal on Numerical Analysis* 2002; **39**(5):1749–1779.
13. Castillo P. Performance of discontinuous Galerkin methods for elliptic PDEs. *SIAM Journal on Scientific Computing* 2002; **24**(2):524–547.
14. Embar A, Dolbow J, Harari I. Imposing Dirichlet boundary conditions with Nitsche's method and spline-based finite elements. *International Journal for Numerical Methods in Engineering* 2010; **83**:877–898.
15. Griebel M, Schweitzer MA. A particle-partition of unity method – part V: boundary conditions. In *Geometric Analysis and Nonlinear Partial Differential Equations*, Hildebrandt S, Karcher H (eds). Springer-Verlag: Berlin, 2002; 517–540.
16. Hansbo A, Hansbo P. An unfitted finite element method, based on Nitsche's method, for elliptic interface problems. *Computer Methods in Applied Mechanics and Engineering* 2002; **191**(47):5537–5552.
17. Dolbow JE, Franca LP. Residual-free bubbles for embedded Dirichlet problems. *Computer Methods in Applied Mechanics and Engineering* 2008; **197**(45):3751–3759.
18. Mourad HM, Dolbow J, Harari I. A bubble-stabilized finite element method for Dirichlet constraints on embedded interfaces. *International Journal for Numerical Methods in Engineering* 2007; **69**(4):772–793.
19. Truster TJ, Masud A. Primal interface formulation for coupling multiple PDEs: a consistent derivation via the variational multiscale method. *Computer Methods in Applied Mechanics and Engineering* 2014; **268**:194–224.
20. Eyck AT, Celiker F, Lew A. Adaptive stabilization of discontinuous Galerkin methods for nonlinear elasticity: motivation, formulation, and numerical examples. *Computer Methods in Applied Mechanics and Engineering* 2008; **197**(45):3605–3622.
21. Liu R, Wheeler MF, Yotov I. On the spatial formulation of discontinuous Galerkin methods for finite elastoplasticity. *Computer Methods in Applied Mechanics and Engineering* 2012; **253**:219–236.
22. McBride AT, Reddy BD. A discontinuous Galerkin formulation for gradient plasticity at finite strains. *Computer Methods in Applied Mechanics and Engineering* 2009; **198**:1805–1820.
23. Nguyen VD, Becker G, Noels L. Multiscale computational homogenization methods with a gradient enhanced scheme based on the discontinuous Galerkin formulation. *Computer Methods in Applied Mechanics and Engineering* 2013; **260**:63–77.
24. Noels L, Radovitzky R. A general discontinuous Galerkin method for finite hyperelasticity. Formulation and numerical applications. *International Journal for Numerical Methods in Engineering* 2006; **68**(1):64–97.
25. Whiteley JP. Discontinuous Galerkin finite element methods for incompressible non-linear elasticity. *Computer Methods in Applied Mechanics and Engineering* 2009; **198**(41):3464–3478.

26. Sanders J, Puso MA. An embedded mesh method for treating overlapping finite element meshes. *International Journal for Numerical Methods in Engineering* 2012; **91**(3):289–305.
27. Eyck AT, Celiker F, Lew A. Adaptive stabilization of discontinuous Galerkin methods for nonlinear elasticity: analytical estimates. *Computer Methods in Applied Mechanics and Engineering* 2008; **197**(33-40):2989–3000.
28. Ortner C, Süli E. Discontinuous Galerkin finite element approximation of nonlinear second-order elliptic and hyperbolic systems. *SIAM Journal on Numerical Analysis* 2007; **45**:1370–1397.
29. Belytschko T, Liu WK, Moran B, Elkhodary K. *Nonlinear Finite Elements for Continua and Structures*. Wiley: Hoboken, New Jersey, 2014.
30. Laursen TA. *Computational Contact and Impact Mechanics*. Springer, 2003.
31. Brezzi F, Fortin M. *Mixed and Hybrid Finite Element Methods*, Vol. 15. Springer-Verlag: New York, 1991.
32. Nistor I, Guiton MLE, Massin P, Moës N, Géniaut S. An X-FEM approach for large sliding contact along discontinuities. *International Journal for Numerical Methods in Engineering* 2009; **78**:1407–1435.
33. Hautefeuille M, Annavarapu C, Dolbow JE. Robust imposition of Dirichlet boundary conditions on embedded surfaces. *International Journal for Numerical Methods in Engineering* 2012; **90**(1):40–64.
34. Masud A, Scovazzi G. A heterogeneous multiscale modeling framework for hierarchical systems of partial differential equations. *International Journal for Numerical Methods in Fluids* 2011; **65**(1-3):28–42.
35. Masud A, Truster TJ. A framework for residual-based stabilization of incompressible finite elasticity: stabilized formulations and F̄-methods for linear triangles and tetrahedra. *Computer Methods in Applied Mechanics and Engineering* 2013; **267**:359–399.
36. Hughes TJR. Multiscale phenomena: Green's functions, the Dirichlet-to-Neumann formulation, subgrid scale models, bubbles and the origins of stabilized methods. *Computer Methods in Applied Mechanics and Engineering* 1995; **127**(1-4):387–401.
37. Masud A, Kaiming X. A stabilized mixed finite element method for nearly incompressible elasticity. *Journal of Applied Mechanics* 2005; **72**(5):711–720.
38. Masud A, Truster TJ, Bergman LA. A variational multiscale a posteriori error estimation method for mixed form of nearly incompressible elasticity. *Computer Methods in Applied Mechanics and Engineering* 2011; **200**(47–48): 3453–3481.
39. Masud A, Calderer R. A variational multiscale method for incompressible turbulent flows: bubble functions and fine scale fields. *Computer Methods in Applied Mechanics and Engineering* 2011; **200**(33):2577–2593.
40. Masud A, Khurram RA. A multiscale/stabilized finite element method for the advection–diffusion equation. *Computer Methods in Applied Mechanics and Engineering* 2004; **193**(21):1997–2018.
41. Marsden JE, Hughes TJR. *Mathematical Foundations of Elasticity (Dover Civil and Mechanical Engineering)*. Dover Publications: Mineola, New York, 1994.
42. Simo JC, Armero F. Geometrically non-linear enhanced strain mixed methods and the method of incompatible modes. *International Journal for Numerical Methods in Engineering* 1992; **33**(7):1413–1449.
43. Radovitzky R, Seagraves A, Tupek M, Noels L. A scalable 3D fracture and fragmentation algorithm based on a hybrid, discontinuous Galerkin, cohesive element method. *Computer Methods in Applied Mechanics and Engineering* 2011; **200**(1-4):326–344.
44. Simo JC, Taylor RL, Pister KS. Variational and projection methods for the volume constraint in finite deformation elasto-plasticity. *Computer Methods in Applied Mechanics and Engineering* 1985; **51**(1):177–208.
45. Brezzi F, Bristeau M-O, Franca LP, Mallet M, Rogé G. A relationship between stabilized finite element methods and the Galerkin method with bubble functions. *Computer Methods in Applied Mechanics and Engineering* 1992; **96**(1):117–129.
46. Ogden RW. *Non-linear Elastic Deformations*. Dover Publications: Mineola, New York, 1997.